The mercury imaging X-ray spectrometer (MIXS) on BepiColombo

Journal Item

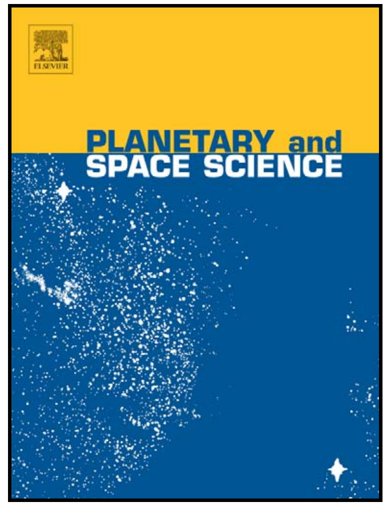

www.elsevier.com/locate/pss

The mercury imaging X-ray spectrometer (MIXS) on BepiColombo

G.W. Fraser, J.D. Carpenter, D.A. Rothery, J.F. Pearson, A. Martindale, J. Huovelin, J. Treis, M. Anand, M. Anttila, M. Ashcroft, J. Benkoff, P. Bland, A. Bowyer, A. Bradley, J. Bridges, C. Brown, C. Bulloch, E.J. Bunce, U. Christensen, M. Evans, R. Fairbend, M. Feasey, F. Giannini, S. Hermann, M. Hesse, M. Hilchenbach, T. Jorden, K. Joy, M. Kaipiainen, I. Kitchingman, P. Lechner, G. Lutz, A. Malkki, K. Muinonen, J. Näränen, P. Portin, M. Prydderch, J. San Juan, E. Sclater, E. Schyns, T.J. Stevenson, L. Strüder, M. Syrjasuo, D. Talboys, P. Thomas, C. Whitford, S. Whitehead

PII: S0032-0633(09)00148-2
DOI: doi:10.1016/j.pss.2009.05.004
Reference: PSS 2672

To appear in: *Planetary and Space Science*

Received date: 11 February 2008
Revised date: 2 April 2009
Accepted date: 7 May 2009

Cite this article as: G.W. Fraser, J.D. Carpenter, D.A. Rothery, J.F. Pearson, A. Martindale, J. Huovelin, J. Treis, M. Anand, M. Anttila, M. Ashcroft, J. Benkoff, P. Bland, A. Bowyer, A. Bradley, J. Bridges, C. Brown, C. Bulloch, E.J. Bunce, U. Christensen, M. Evans, R. Fairbend, M. Feasey, F. Giannini, S. Hermann, M. Hesse, M. Hilchenbach, T. Jorden, K. Joy, M. Kaipiainen, I. Kitchingman, P. Lechner, G. Lutz, A. Malkki, K. Muinonen, J. Näränen, P. Portin, M. Prydderch, J. San Juan, E. Sclater, E. Schyns, T.J. Stevenson, L. Strüder, M. Syrjasuo, D. Talboys, P. Thomas, C. Whitford and S. Whitehead, The mercury imaging X-ray spectrometer (MIXS) on BepiColombo, *Planetary and Space Science*, doi:10.1016/j.pss.2009.05.004

The Mercury Imaging X-ray Spectrometer (MIXS) on BepiColombo

G.W. Fraser[1*], J.D. Carpenter[1], D.A. Rothery[2], J.F. Pearson[1], A. Martindale[1], J. Huovelin[3], J. Treis[4,5], M. Anand[2], M. Anttila[6], M. Ashcroft[7], J. Benkoff[8], Bland, P.[9], A. Bowyer[7], A. Bradley[7], J. Bridges[1], C. Brown[1], C. Bulloch[7], E.J. Bunce[1], U. Christensen[4], M. Evans[1], R. Fairbend[10], M. Feasey[7], F. Giannini[8], S. Hermann[11,5], M. Hesse[12], M. Hilchenbach[4], T. Jorden[13], K. Joy[14,15], M. Kaipiainen[16], I. Kitchingman[7], P. Lechner[17,5], G. Lutz[17,5], A. Malkki[18], K. Muinonen[3], J. Näränen[3], P. Portin[19], M. Prydderch[15], J. San Juan[20], E. Sclater[7], E. Schyns[10], T.J. Stevenson[1], L. Strüder[11,5], M. Syrjasuo[18], D. Talboys[1], P. Thomas[7], C. Whitford[1], S. Whitehead[7].

[1]Space Research Centre, Department of Physics and Astronomy, University of Leicester, University Road, Leicester, LE1 7RH, UK

[2]Department of Earth and Environmental Sciences, The Open University, Walton Hall, Milton Keynes, MK7 6AA, Milton Keynes, UK

[3]University of Helsinki Observatory, University of Helsinki, 00014 Helsinki, Finland

[4]Max Planck Institute for Solar System Research, Max-Planck-Str. 2, 37191 Katlenburg-Lindau, Germany

[5] Max Planck Institute Halbleiterlabor, Otto-Hahn-Ring 6, 81739 Munich, Germany

[6]Space Systems Finland Ltd., Kappelitie 6 B, 02200 Espoo, Finland

[7]Magna Parva Ltd, Loughborough Innovation Centre, Epinal Way, Loughborough, Leicestershire, LE11 3EH

[8]ESA/ESTEC, Keplerlaan 1, Postbus 299, 2200 AG, Noordwijk, The Netherlands.

[9] Impacts and Astromaterials Research Centre, Department of Earth Science and Engineering, Imperial College London, South Kensington Campus, London SW7 2AZ, UK.

[10]Photonis SAS, Av. Roger Roncier BP520, 19106 Brive cedex, France

[11]Max Planck Institute für Extraterrestrische Physik, Giessenbachstraße, 85748 Garching, Germany

[12] Centro de Astrobiología (CSIC/INTA), Instituto Nacional de Técnica Aeroespacial, Ctra de Torrejón a Ajalvir, km 4, 28850 Torrejón de Ardoz, Madrid, Spain

[13]EADS Astrium Ltd, Gunnels Wood Road, Stevenage, SG1 2AS, UK

[14]UCL/Birkbeck Research School of Earth Sciences, UCL, Gower Street, London, WC1E 6BT, UK.

[15]Rutherford Appleton Laboratory, Harwell Science and Innovation Campus, Didcot, Oxfordshire, OX11 0QX, UK

[16]Oxford Instruments Analytical Oy, PO Box 85 (Nihtisillankuja 5), Fin-02361 Espoo, Finland

[17]PNSensor GmbH, Römerstrasse 28, 80803, Munich, Germany

[18]Finnish Meteorological Institute, Erik Palménin Aukio, FI-00560, Helsinki, Finland

[19]Patria Aviation OY, Naulakatu 3, FI-33100, Tampere, Finland

[20]LIDAX, Ax. Cristóbal Colón 16, 28850 Torrejon de Ardoz, Madrid, Spain

*e-mail: gwf@star.le.ac.uk

Telephone: +44 (0) 116 252 3542

Fax: +44 (0) 116 252 2464

Abstract

The Mercury Imaging X-ray Spectrometer (MIXS) on the BepiColombo Mercury Planetary Orbiter (MPO), will measure fluorescent X-ray emission from the surface of Mercury in the energy range 0.5 – 7.5 keV, which is induced by incident solar X-rays and solar wind electrons and protons. These X-rays will reveal the elemental composition of the surface of Mercury and aid the determination of the planet's evolution.

MIXS is a two component instrument. A collimated channel (MIXS-C) provides measurements on scales of 70-270 km, sufficient to separate the major Mercurian terrains. A second channel (MIXS-T) is the first imaging X-ray telescope for planetary remote sensing and will make measurements on spatial scales of less than 10 km for major elements during solar flares, sufficient to isolate surface landforms, such as craters and their internal structures. The spatial resolution achieved by MIXS-T is made possible by novel, low mass microchannel plate X-ray optics, in a Wolter type I optical geometry.

MIXS measurements of surface elemental composition will help determine rock types, the evolution of the surface and ultimately a probable formation process for the planet. In this paper we present MIXS and its predicted performance at Mercury as well as discussing the role that MIXS measurements will play in answering the major questions about Mercury.

Keywords

Mercury; BepiColombo; X-ray fluorescence; composition; instrumentation

1 Introduction

The innermost planet, Mercury represents an end member of the solar system in terms of size, metal-to-silicate ratio and probably conditions of formation. Knowledge of Mercury's history and formation is therefore essential to understand the formation and evolution of the inner solar system as a whole. Mercury is also the least explored of all the planets. Until recently, three brief flybys by Mariner 10 in 1974 and 1975 provided the only detailed measurements of the planet. At the time of writing (January 2008) the first data is being returned from NASA's MESSENGER mission to Mercury, which flew by the planet on 14th January 2008. Following additional flybys in October 2008 and September 2009, MESSENGER will ultimately go into orbit around Mercury in 2011. These data, coupled with ground based measurements, have provided a picture of an anomalously dense, airless and heavily cratered world which superficially resembles the Moon. Mercury's very large core and an apparent paucity of iron at the surface (estimated, on the basis of ground-based spectroscopy, at less than 3 wt % FeO) are only two of the more striking differences between the two bodies (Strom and Sprague, 2003; Solomon, 2003).

The major unanswered questions at Mercury may be divided into two categories

Primary questions:

- From what material did Mercury form, and how?
- How and when did Mercury become internally differentiated?

- Is there both primary and secondary crust on Mercury (as defined by Taylor, 1989)?
- Why does Mercury have a dipole magnetic field?

Secondary questions:

- What is the history of crustal evolution on Mercury?
- What is the crustal composition and how does it vary (i) across the surface, (ii) with depth?
- How are the surface and exosphere related?
- How do the surface and magnetosphere interact?
- Does Mercury have a molten core?
- What are the deposits observed in craters near to the poles?

The Mercury Imaging X-ray Spectrometer (MIXS) on BepiColombo Mercury Planetary Orbiter (MPO) will measure fluorescent X-rays from the surface of Mercury. Fluorescent X-rays reveal the elemental composition of the surface to depths of a few micrometres for low atomic number elements such as magnesium and for the L-shell emission lines of heavier elements. For the harder, K-shell emission lines of heavier elements, measurements of the fluorescent X-rays probes a deeper layer of the planetary surface (of order tens of microns). Measurement of the composition of the regolith in this way is a tool for determining the geological history and ultimately the formation mechanisms for the planet. X-ray spectroscopy is complementary to measurements at optical and infrared wavelengths which indicate chemical bonding and mineralogy, and to gamma ray and neutron measurements which provide low spatial resolution measurements of certain elements at depths of approximately 10 cm. In this paper we describe the production of X-rays on Mercury's surface, the MIXS instrument and its capabilities and the expected contribution that measurements by MIXS will make towards answering the major questions about Mercury.

2 X-ray remote sensing

X-ray fluorescence has been used for remote sensing on Apollo 15 and 16 at the Moon (Adler et al., 1973), on the Near Earth Asteroid Rendezvous (NEAR Shoemaker) mission to asteroid 433 Eros (Trombka et al., 2000), on the Hayabusa mission to asteroid 25143 Itokawa (Okada et al., 2006) and on the SMART-1 mission to the Moon (Grande et al., 2003). The Chandrayaan 1 and Kaguya (Selene) missions to the Moon also carry X-ray spectrometers (Grande et al., 2008 and Shirai et al. 2008). The X-ray spectrometer on MESSENGER (Leary et al., 2007) is derived from those on Apollo and NEAR Shoemaker and uses collimated gas proportional counters as the detectors of X-rays (Schlemm et al., 2007). The instruments on SMART-1 and Chandrayaan 1 were based on silicon Swept Charge Device (SCD) detectors (Lowe et al., 2001), while those on Hayabusa and Kaguya use silicon Charge Coupled Device (CCD) detectors. The detectors on MESSENGER have an energy resolution of ~ 880 eV Full Width at Half Maximum (FWHM) at 5.9 keV (Schlemm et al., 2007) and, as was the case for Apollo before them, the separation of the K shell emission lines from Mg (1.25 keV), Al (1.49 keV) and Si (1.74 keV) is not possible. Instead, three separate detectors are employed with thin Be windows, two of which bear an additional thin Mg or Al filter. The differential X-ray attenuation of the three counters is then used to infer the relative heights of the three peaks and produce elemental abundance ratios. The MESSENGER X-ray spectrometer's field of view (FOV) is selected by a 12º collimator which, when coupled with the highly elliptical orbit, results in a surface footprint of approximately 3000 km at apoherm (15193 km), and 40 km at periherm (200 km), the later resolution being available for approximately 15 minutes in each 12 hour orbit. (Schlemm et al., 2007).

MIXS differs radically from previous X-ray instruments for planetary remote sensing, offering unprecedented spectral and spatial resolutions. MIXS has two complementary instrument channels shown in Figure 1; MIXS-C (collimator) and MIXS-T (telescope). MIXS-C has a 10.4° Field Of View (FOV), which defines its angular resolution, and is optimised to provide the largest X-ray throughput at all energies and for all solar states. The MIXS-C FOV results in a surface pixel size of 70 km at periherm (400 km orbital altitude) and 270 km at apoherm (1500 km orbital altitude). MIXS-T is an imaging X-ray telescope with a 1.1° FOV and has an angular resolution better than 9 arc minutes, which may be used to full effect during solar flares when the incident (and thence the fluorescent) X-ray flux is highest. MIXS-T's angular resolution is sufficient to provide a spatial resolution better than 1 km at periherm and 4 km at apoherm. Together these two channels ensure comprehensive measurements of the compositions of the major terrains and, where solar conditions allow, the compositions of landform elements such as crater peaks at spatial scales less than 10 km.

3 The relationship between Mercury's composition and its formation

Mercury has an extraordinarily large uncompressed density (5.3 g cm^{-3} compared with 4.0 g cm^{-3} for Earth), which is incompatible with models of formation by equilibrium condensation (Cameron et al., 1988) and indicates that Mercury's metallic mass fraction is at least twice that of the other terrestrial planets (Solomon, 2003). A large iron-rich core is postulated, which occupies about 42% of the planet's volume and 75% of the radius and there is evidence that it is at least partly molten (Margot et al., 2007).

Several models have been proposed to explain the relative sizes of Mercury's core and its silicate fraction (mantle plus crust). These models fall into three basic categories: selective accretion, post accretion vaporisation and massive impact.

In the first of these models, the oxidation gradient during solar nebula condensation, aided by gravitational and drag forces, resulted in an enrichment of metallic iron compared with other terrestrial planets (Weidenschilling, 1978). In the second, intense solar radiation in the early Solar System led to the vaporisation and loss of silicates from Mercury's exterior after the planet had formed (Cameron, 1985), or possibly from the differentiated exteriors of planetary embryos before they collided to form Mercury. In the latter model, a giant impact stripped Mercury of much of its rocky exterior (Benz et al., 1988, 2007). A range of credible compositions for Mercury's mantle plus crust, which result from the proposed models, is tabulated in Table 1.

4 Crust formation on Mercury and effects on surface elemental composition

The measured abundance of elements on Mercury's surface cannot, however, be representative of the bulk silicate fraction (mantle plus crust). The crust, whether "primary" or "secondary" (Taylor, 1989) or both, must be chemically differentiated from the mantle by processes dependent on its emplacement mechanisms. Space weathering may further change the surface elemental abundances, so none of the models in Table 1 is likely to correspond to the detected surface composition.

Primary crust is the oldest surviving crust, and would have derived from a magma ocean (a highly-likely eventuality in any planetary growth scenario involving embryo-embryo collision and/or a final 'giant impact'). Primary crust would be comprised of minerals that grew by fractional crystallisation from a magma ocean melt of mantle (bulk silicate) composition and floated to the surface. This crustal material would be analogous to, and enriched in certain elements in ways comparable to, the anorthosites of the lunar highlands which are enriched in Al and Ca relative to the mantle's bulk composition. Na may be enriched to detectable concentrations in primary crust, although Na concentrations are less than 1.5% in lunar anorthosites, and both Fe and Mg would be depleted. The final crystallisation products of a magma ocean would be expected to have enrichments in the incompatible elements such as K and the rare Earth elements, analogous to the KREEP (Potassium, Rare Earth Elements and Phosphorus) component identified on the Moon.

Secondary crust results from partial melting in the mantle and will have been emplaced volcanically. Secondary crust will tend to be enriched in Fe (Robinson and Taylor, 2001) but depleted in Mg relative to the bulk composition. Secondary crust will also have a greater abundance of Al, Ca and Na than the mantle (but less than primary crust), and will be richer in K, Ti and Cr than any other major silicate component of the planet. Silicon abundance will probably be less in secondary crust than in primary crust, but the fractional change in Si abundance between crustal types will be small compared to that for other elements, depending on the extent of partial melting. Material erupted after storage and differentiation in large-volume basaltic magma chambers will be lower in Fe and Ti but richer in alkalis than in directly-erupted basalts (Jeanloz et al., 1995).

Extensive tracts of exposed primary crust on Mercury have yet to be identified. The planet's surface may prove to be largely secondary crust, but it will be important to identify and characterise any exposures of primary crust that have survived resurfacing (or have been re-exposed through tectonism or impact cratering). With the understanding that the Moon is not necessarily a close analogue for Mercury, we present data in Table 2 to indicate the sorts of variation in crustal composition at Mercury that an instrument such as MIXS needs to be able to measure. The diagnostic significance of the elements shown in Table 2 is discussed further in Section 5 of this paper.

Long-term exposure to meteorite impacts and energetic particles may further alter surface elemental abundances, by processes often described as 'space weathering'. One consequence of this may be the reduction of Fe bonded to oxygen within silicates to metallic 'nanophase iron', alternatively known as submicroscopic metallic iron (SMFe) particles (Blewett et al., 2002). Infrared – ultraviolet spectroscopy is not sensitive to metallic Fe and so X-ray spectroscopy provides the only mechanism for detection of Fe in SMFes. These provide a possible explanation for the apparent deficiency of Fe in surface minerals. MIXS is therefore a crucial complement to the optical and infrared spectrometers on BepiColombo (Simbio-Sys (this issue) and MERTIS (this issue)).

Determination of Mercury's bulk silicate composition on the basis of surface measurements requires the identification and understanding of the history of crust formation and of the subsequent surface processes. This requires a combination of elemental analysis by X-ray, neutron and gamma ray spectroscopy, visual interpretation of geological features on high-resolution optical images, and infrared – ultraviolet spectroscopy to infer mineralogy.

5 The importance of different elements at Mercury

The following arguments describe the diagnostic significance of various elements whose fluorescent X-ray emission is within the energy range detectable by MIXS.

Si: Expected in a narrow range, 19-25% (15–33% in some lunar specimens). Si as a stand-alone element is unlikely to allow determination of mechanisms for Mercury's formation or the evolution of the surface but is useful, not least as a reference to which other elements may be compared.

Ti: Between 1% and 8% in lunar and terrestrial basalts. Abundances greater than 3% on Mercury would indicate sufficient oxygen fugacity to form Ti-oxides (as opposed to Ti merely substituting for other cations within silicates). A Ti abundance of approximately 0.1% or less in lavas would support an enstatite chondrite model for Mercury's composition (Taylor and Scott, 2004).

Al: By analogy with the Moon, expected to be abundant in primary crust (~18%), but between 4% and 10% in basalts. Distinguishing between, for example, 18% and 10% Al content would allow the separation of primary and secondary crust.

Fe: The confirmation or otherwise of a low Fe abundance in Mercury's crust is of key importance. Fe abundance is expected to be less than 2% in primary crust, but could be at least 4% in secondary crust. Fe concentration of less than 0.3% would support an enstatite chondrite origin for Mercury's composition (Taylor and Scott, 2004).

Mg: Should be rare in primary crust (less than 2%), but abundant (4-12%) in secondary crust unless the outer part of Mercury has been stripped to reveal inner mantle Mg-rich cumulate. A Magnesium concentration less than 7% would support a refractory-volatile mixture model of Mercury, whereas more than 10% in lavas would support other models (Taylor & Scott, 2004).

Na: Possibly as much as 1% in primary crust and expected to be less abundant in most basalts, although some terrestrial basalts contain more than 1% Na. Detection of Na would place constraints on the volatile budget within Mercury. The liberation of Na into the exosphere from surface material may occur through interplanetary dust impacts, large impacts and the subsequent exposure of fresh regolith, thermal desorption and evaporation, recycling processes from cold craters and ion sputtering.

Ca: By analogy with the Moon, Ca should be abundant in primary crust (18-20%) but rarer in secondary crust (8-14%). A Ca concentration of less than 9% in units recognised as lava would support an enstatite chondrite model of Mercury's composition (Taylor and Scott, 2004). Like Na, Ca is also a constituent of Mercury's exosphere.

P: Reaches concentrations of about 0.1% in lunar mare basalts and double that in the petrologically significant KREEP basalts of the lunar highlands. P and Ti have similar partitioning behaviour during partial melting, and the Ti/P ratio in chondrites is about 1. Thus, a Ti/P of order 10 in volcanic terrains on Mercury would indicate previous scavenging of P into the core and thus provide compelling confirmation of Mercury core formation prior to volcanism.

Mn: Reaches about 0.3% in lunar mare basalts but is much less abundant in primary crust. If detectable on Mercury, it would be expected in secondary crust only.

K: Effectively absent in lunar primary crust, but up to as much as 1% in some kinds of lunar secondary crust and higher in some impact melts. If detected on Mercury, potassium may be used in conjunction with other elements to constrain basalt petrogenesis. K is also a major component of the exosphere.

S: Fe sulphides could provide the sulphur observed in the exosphere and inferred from radar backscatter from Mercury's poles (Sprague et al., 1995, 1996). S concentration is probably much less than 1% except possibly in areas of high-radar reflectivity in polar craters, where sulphur is an alternative candidate to water ice for the material making up the reflective layer. X-ray emission from S inside polar craters would have to be induced by incident electrons (and/or protons) in the absence of direct illumination by the Sun.

Cr: Averages 500 – 600 ppm in the lunar crust. Cr of order 1% in rocks identified as lava would support a refractory-volatile mixture model of Mercury, whereas 0.1% would support other models (Taylor and Scott, 2004).

Ni: Present in abundances less than 400 ppm in the lunar crust, and potentially diagnostic in conjunction with Cr. On the Moon the Cr:Ni abundance ratio has been used to constrain formation models (Taylor, 1975).

O: It is conventionally assumed that in silicate rocks cations (all elements in Table 2 apart from S) are oxidised. O is therefore likely to be about 44-46% in surface materials. A significant departure from this abundance would call into question the whole mineralogy of Mercury's crust.

In addition, the acquisition of volatile elements will indicate whether Mercury conforms to the approximate trend of increasing depletion with decreasing heliocentric distance, defined by C-type asteroids in the outer belt, to S-type, to E-type in the inner belt, to Mars, to Earth (Bland and Benedix, 2006). Determining volatile abundances will also allow constraints to be placed on volatile depletion during a putative giant impact.

6 Solar X-ray induced fluorescence from Mercury's surface

The primary mechanism for producing X-ray fluorescence from airless planetary bodies in the inner solar system, within approximately 3 AU of the Sun (Adler and Trombka, 1970; Adler et al., 1972), is excitation by solar coronal X-rays, although fluorescence can also be induced through bombardment by charged particles. Solar X-ray induced X-ray fluorescence spectroscopy as an observational technique is therefore limited to the Moon, Mercury, asteroids and comets in the inner solar system.

The intensity of X-ray fluorescence from the various elements on a planet's surface depends on the energy and intensity of incident solar X-rays, but solar X-ray intensity can vary by several orders of magnitude and can be highly variable on time scales of minutes. It is therefore essential that measurements of planetary fluorescent X-ray emission are accompanied by simultaneous measurements of the solar X-ray spectrum. On BepiColombo, solar X-rays will be measured by the Solar Intensity X-ray and Particle Spectrometer, SIXS (Huovelin et al., this volume), which also characterises the particle environment local to the spacecraft. These measurements by SIXS allow normalisation of fluorescence measurements from different orbits allowing the correction of data in order to give a self-consistent picture of the surface.

Figure 2 shows the solar X-ray flux as a function of energy for various solar flare states measured at 1 AU by the X-ray Solar Monitor (XSM) on SMART 1 (Huovelin et al., 2002). Solar flare states are defined according to the total energy output of the sun measured in the wavelength range 1-8 Å, as measured by the NOAA's GOES spacecraft, in orbit around the Earth. Flare states are designated as : solar quiet (A1 flare), B, C, M or X on a scale where an X1 flare is 10 times an M1 flare is 10 times a C1 flare etc. The largest solar flare to date, in November 2003, is believed to have peaked at around X40 (Brodrick et al., 2005). Also shown in Figure 2 are polynomial approximations to solar spectra taken from Truscott et al. (2000). The polynomial approximation to the solar quiet spectrum below 4 keV is smoothed and extrapolated from the 0.3-2.7 keV spectrum reported by Fichtel and Trombka (1997) who in turn used earlier (semi-empirical) work by Tucker and Koren (1971) based on observations from Apollo 15. Above 4 keV, data from Clark et al. (1997) are added. Line emissions were not included in these spectra because the hotter the solar coronal plasma (i.e. the more active the Sun), the more the total continuum emission will dominate. Nevertheless, Tucker and Koren (1971) include more than 450 lines in their solar coronal model; these lines will be included in future MIXS calculations. The detection of lines in the measured solar spectra of Figure 2 is limited by the spectral resolution of the XSM detector. The Fe-Kα line is resolved in the M-flare XSM data at 6.6 keV, shifted from 6.4 keV for cold iron because of the increased ionization state for Fe in the solar corona.

The solar spectrum will be scattered from the planetary surface as well as initiating fluorescence. However, the energy resolution of the MIXS instrument will allow it to detect the shift in energy between elastically and inelastically scattered X-ray line emission. The XSM "C1 flare" data shown in Figure 2 was recorded during a C2 flare event and reduced by a factor of 2. The divergence of the XSM solar quiet data from its representative polynomial, above 4 keV, is probably due to the inclusion of the diffuse X-ray background (DXB) and galactic X-ray background within the 52° XSM field view. The predicted contribution to the measured flux due to the DXB (whose intensity is given by Zombeck, 2007) is also shown in Figure 2.

BepiColombo will arrive at Mercury shortly after solar minimum in August 2019, with a nominal mission duration of 1 year, extensible to 2 years. Representing the years of operation at Mercury with the corresponding years, two solar cycles earlier, around solar minimum in 1997, we can estimate the fractions of a year for which the Sun is expected in various flare states in 2019 and 2020 (Huovelin et al. (this volume)).

If E is the X-ray energy and the incident intensity of parallel solar X-rays on Mercury's surface is $I_0(E)$ (photons cm^{-2} s^{-1}) then the intensity of fluorescence from a given X-ray line (photons cm^{-2} s^{-1} steradian^{-1}) can be determined in terms of fundamental physical parameters by the relationship shown in Equation 1, adapted from Clark and Trombka (1997).

$$I_{line} = \frac{1}{4\pi} w_i g C_i \left(\frac{r-1}{r}\right) \int_{E_{abs}}^{\infty} I_0(E) \rho \cos\theta \frac{\left(\frac{\mu(E)_i}{\rho_i}\right)}{\mu(E) + \mu(E_{line}) \frac{\cos\theta}{\cos\phi}} dE \qquad (1)$$

where w_i is the fluorescence yield of a given emission series (K,L etc.), g is the weight fraction of a given line within a series (α, β etc.), C_i is the mass fraction of a given element, r is the jump ratio at the absorption edge of interest, ρ is the bulk density of the surface material, ρ_i is the partial density of the element of interest, θ is the angle of incidence of the incident solar X-rays, measured from the surface normal and ϕ is the viewing angle measured from the surface normal. $\mu(E)$ is the mass absorption coefficient of the bulk material and $\mu(E)_i$ is the linear absorption coefficient for the element of interest. E_{line} is the energy of the elemental emission line of interest.

Equation 1 assumes a perfectly smooth and homogeneous planar surface; no allowance is made for effects due to the real properties of the planetary regolith, including surface roughness and packing density. Also unaccounted for in Equation 1 are shadowing effects due to large scale topography. Energy independent effects of the regolith and topography (e.g. shadowing) may be removed by the use of elemental abundance ratios (e.g. Mg:Si, Al:Si) instead of absolute abundances, however the use of ratios cannot remove any effects for which there is an energy dependency, and it has been shown in preliminary measurements that for large values of θ and ϕ the measured ratios of elemental line intensities varies as a function of surface roughness by 10% - 20% (Näränen et al., 2007,Okada et.al, 2004). Work is continuing at the University of Leicester, the University of Helsinki and Birkbeck College to quantify the effects of regolith properties on line intensities, in order to provide a more complete interpretation of X-ray fluorescence data from planetary surfaces.

To indicate the fluorescence emission spectrum expected from Mercury's surface, line emissions calculated from Equation 1 are shown in Figure 3. Solar input spectra for the simulation are the polynomials shown in Figure 2, scaled to an average Mercury-Sun separation of 0.39 AU. Also shown in Figure 3 is the scattered X-ray continuum, calculated using Equations 2 – 9 of Clark and Trombka (1997). The surface is simulated as a smooth high-K lunar basalt with a composition given by Taylor (1975) (Table 2). A lunar basalt composition may not be a close analogue for much of Mercury's surface, but basalt contains a rich mix of elements and is used here to give an indication of the fluorescence intensities that might be expected from the various elemental lines of interest. The lines shown are for solar quiet, B1, C1, and M1 flare states. The ability of MIXS to resolve individual lines is discussed in Section 10.

7 Magnetospheric Phenomena and X-ray emission

X-ray emission may also result directly from magnetospheric phenomena (for reviews of Mercury's magnetosphere see Ness, 1979; Russell et al., 1988; Slavin, 2004; Milillo et al., 2005). Mariner 10 showed that Mercury has a largely dipolar magnetic field tilted only slightly to the planetary spin axis. Interaction of this magnetic field with the solar wind creates a miniature magnetosphere, capable of standing off the solar wind to a distance of ~1.5 R_M (where 1 R_M is 2439 km). However, the nature of the internal dynamo is yet to be fully understood. Nevertheless, Mariner 10 observations left the impression that Mercury's magnetosphere is potentially one of the most dynamic in the solar system, showing evidence of familiar terrestrial magnetospheric processes. These include dayside magnetic reconnection phenomena (or Flux Transfer Events - FTEs) similar to those seen at the Earth, ULF wave activity (indicative of closed field lines), and extremely rapid substorm activity on time-scales of a few tens of seconds. It is possible that these processes will produce X-rays at the surface of the planet (or even in the exosphere) due to precipitation and/or acceleration of electrons and/or ions in large scale current systems associated with solar wind-magnetosphere-exosphere-surface coupling (for example, see Grande, 1997; Burbine et al., 2005). Burbine et al. (2005) have suggested that electron-induced X-ray emission from Mg, Al and Si should be detectable by the MESSENGER X-ray Spectrometer (XRS) on the dark side of Mercury.

If this is the case, MIXS would sample the surface/exosphere effects of this dynamic coupling, which *in situ* plasma and field measurements alone will not be able to establish. Candidate processes which may produce surface X-ray emission are: cusp dynamics or FTEs, substorms/Pi2 pulsations (irregular and damped ultralow frequency range magnetic pulsations which occur in connection with magnetospheric substorms), and the effects of active solar wind conditions (i.e. Solar Energetic Proton events (SEPs) and Coronal Mass Ejections (CMEs)). To fully understand the magnetospheric phenomena, of which X-ray emission is one manifestation, it will be important to coordinate measurements by MIXS with *in situ* field and plasma measurements taken with instruments on both the MMO and MPO spacecraft.

8 The Mercury Imaging X-ray Spectrometer (MIXS)

The optical elements for both instrument channels, shown schematically in Figure 1, consist of microchannel plate (MCP) X-ray optics operating in two different modes and manufactured by Photonis SAS (Brive, France). MIXS-T has radially packed, square-pore MCPs in a Wolter Type I optical geometry (Willingale et al., 1998). MIXS-C has square packed, square-pore MCP optics in a "slumped collimator" optical geometry. Figure 4 shows a scanning electron microscope image of an MCP coated with a thin layer of Ir to optimise its X-ray reflectivity (Jefimovs et al., 2007). The MCPs for both telescope and collimator have a high reflectivity 60 nm thick Al film over their front faces, to reduce thermal load. Microchannels are arranged in square multifibres, which are then stacked in the appropriate geometry.

8.1 The MIXS focal plane assembly

Both MIXS-T and MIXS-C have identical focal plane assemblies, based on monolithic 19.2 mm × 19.2 mm Active Pixel Sensors (APS). The sensor features Macropixels (Zhang et al., 2006), which combine the benefits of DEPFET (DEpleted P-channel Field Effect Transistor) structure (Treis et al., 2006) (i.e. low power consumption, fast readout, excellent energy resolution at low noise, intrinsic radiation hardness and arbitrary access to pixels) with those of a Silicon Drift Detector (SDD) (arbitrary scalable pixel sizes and an entrance window with low X-ray attenuation).

The FWHM energy resolution (ΔE) of the Gaussian detector response is given by

$$\Delta E = 2.36w\left(\frac{FE}{w} + R^2 + A^2\right)^{\frac{1}{2}}, \qquad (2)$$

where w is the energy required to create an electron hole pair (3.62 eV in Si), F is the Fano factor (a factor describing the non-Poissonian variance in the number of electrons generated in a detector by an incident X-ray photon, ~ 0.1 in Si) (Fraser, 1989), E is X-ray energy and R and A are the noise contributions from the readout electronics and amplification (Fraser, 1989). Measurements of X-ray spectra obtained by DEPFET detectors by Zhang et al. (2006) have shown that energy resolutions approaching the theoretical Fano limits (~60 eV at 1 keV, 130 eV at 6 keV) are feasible with these devices.

The MIXS detectors will measure X-rays in the energy range 0.5 – 7.5 keV, with a spectral resolution of 100 eV at 1 keV at the start of operations, following the 6 year cruise to Mercury. The resolution will degrade over the mission lifetime due to radiation damage but should still be less than 200 eV after one year at Mercury (Treis et al., 2008).. This resolution allows the separation of X-ray line emission from elements of interest while the predicted sub-keV quantum efficiency permits the detection of lines not accessible to previous instruments - including the Fe-L emission line at 0.7 keV. This measurement is vital in elucidating the apparent low iron abundance indicated by ground-based visible and infrared spectroscopy (which is sensitive to Fe-O bonds rather than to Fe itself). Fe-L is of particular importance because the higher energy Fe-K lines (6.40 keV and 7.06 keV) are practically visible only during high solar states.

The MIXS focal plane assembly (FPA) consists of a 64×64 array of 300 μm macropixels, each with a triple drift ring structure. Whereas in a charge coupled device (CCD), charge is transferred across the whole device for readout by a single preamplifier, in the macropixel array every pixel has its own readout FET (Field Effect Transistor). The predicted quantum efficiency (QE) of the MIXS detector is shown as a function of energy in Figure 5. The window is 30nm polyimide plus 50nm Al, with negligible X-ray attenuation above 0.5 keV.

8.2 MIXS-C optics

An X-ray collimator is conventionally an array of parallel channels whose aspect ratio (the ratio of channel length L and width d) alone defines the field of view (FOV). The collimator is positioned directly above an underlying detector and the two have identical areas. Such a geometry means that the effective area of a planar collimator falls off linearly with off-axis angle; the angular response is triangular in form (Fraser 1989). In contrast, MIXS-C uses a slumped or radial collimator geometry, shown schematically in Figure 6. This geometry allows (a) the reduction of the required detector size for a given collimator aperture and (b) the physical separation of the collimator and detector planes, with consequent advantages in terms of cost, radiation shielding mass, cooling power and sensitivity.

The MIXS-C collimator is an array of four slumped 40 × 40 mm square pack - square pore glass MCPs with 20μm wide channels. The MCPs are spherically slumped to a common radius of 550 mm and have a channel aspect ratio of 55:1. The open area fraction of the MCPs is 0.6, comparable with that of a standard mechanical collimator. The side length D of the square collimator is 80 mm and the detector is square, with a side length of 19.2mm, identical to the MIXS-T detector. The detector is placed 550 mm from the collimator along the optical axis, at the collimator's centre of curvature. In this geometry, the FOV for collimated X-rays is determined by the sum of the angle subtended by the slumped collimator and the acceptance angle of the channels, and is equal to 10.4°. The design ensures that all X-rays transmitted through the collimator are ultimately incident on the detector.

In addition to the collimated flux , X-rays can be reflected from the Ir-coated internal faces of the microchannels. Figure 7 shows the effective areas (transmitted, transmitted plus reflected rays) as a function of angle for MIXS-C at 1 keV, calculated using the Monte-Carlo raytracing model of Price et al. (2002),. Unlike a conventional collimated instrument, MIXS-C's effective area is constant across most of its FOV. The FOV can be described by two components (i) a core FOV defining the central "flat top" angular response (6.5°) and (ii) the total FOV incorporating the fall-off in effective area to zero (10.4°).

8.3 MIXS-T optics

MIXS-T uses radially-packed, 20 μm square-pore MCP optics, in a conical approximation to the Wolter type I focussing geometry, typically used in X-ray astronomy (Ashenbach, 1985). The MCP embodiment of the Wolter optic geometry is discussed in detail by Willingale et al. (1998); the path of an X-ray through an MCP Wolter pair is illustrated in Figure 8. The focal length of MIXS-T is 1 m, determined by the 4 m and 1.33 m slump radii of the front and rear MCP plates (Willingale et al. 1998). X-rays entering a microchannel in the first plate are reflected at grazing incidence from an internal channel wall, upon exiting the front MCP, the X-ray then enters a microchannel in the rear MCP where a second reflection takes place. After two reflections, the beam converges in the focal plane. Deviations from the optimal path of an X-ray may occur due to multiple reflections within microchannels, misalignments between microchannels and groups of microchannels (multifibres) or because of scattering due to small deviations from a perfectly smooth Ir-coated reflective channel walls. The achievable quality of the focus is ultimately limited by the practical approximation to the radial packing geometry and by the conical approximation to the true Wolter I geometry.

The 210 mm diameter MIXS-T optic, shown in Figure 1 and schematically in Figure 9, is assembled from a mosaic of MCPs, each of which is a sector of a circle, slumped to the figure of the surface of a sphere. Front and rear “sectors” together form “tandems” which are arranged in three rings with different thicknesses (2.2 mm inner, 1.3 mm middle, and 0.9 mm outer) to approximate the ideal 1/r thickness profile which maximises the throughput of the telescope by maximising the probability of a single reflection in each MCP.

The on-axis effective area of the MIXS-T optics has been calculated using a Monte Carlo ray-tracing model incorporating the geometric parameters given above. The mechanical support structure of the telescope, illustrated in Figure 1, is accounted for and perfect stacking of microchannel multifibres is assumed. The on-axis effective area for the MIXS-T optics (not including the detector efficiency) as a function of energy is shown in Figure 10 both for rays which are truly focused (labelled “focussed”) and for all rays incident in the focal plane, including those which undergo scattering or multiple reflections inside the microchannels (labelled “focal plane”). Counting all rays in the focal plane, both focussed and non-focussed, provides a means of maximising the counting rate for any given elemental line, gaining sensitivity at the expense of spatial resolution. Raytracing indicates that the likely limiting resolution for the MIXS-T optics, assuming perfect alignment of microchannels, multifibres and sectors is ~1 arc minute.. The formal science requirement for MIXS-T is to achieve an angular resolution better than 9 arc minutes.

The effective area of MIXS-T decreases with off-axis angle, because the X-ray reflectivity decreases with increased grazing angles to the channel walls, and the reflection geometry along the channels becomes less favourable for single reflections in both front and rear MCPs. This reduction in effective area with off-axis angle is the so-called vignetting function and is shown for four X-ray energies in Figure 11.

8.4 MIXS Grasp

The collecting power of both MIXS channels can be described in terms of the product of effective area and field of view - which in astronomy is known as the Grasp, $G(E)$ (units of cm^2 sr – derived below for a telescope in equation 6). Where X-rays in the energy interval $E,E+dE$ are emitted from an extended source (i.e. the surface of Mercury) and are incident on the instrument aperture with a flux $I(E)$ (in photons cm^{-2} s^{-1} $steradian^{-1}$ keV^{-1}) then the number of detected photons C detected in a time t is given by

$$C = I(E)G(E)tdE \,. \quad (3)$$

The calculated $G(E)$ for MIXS-C shown in Figure 12, is the result of multiplying the field of view (0.033 steradians), by the geometrical area of the collimator (64 cm^2) while taking into account the raytraced transmission of the collimator geometry and the detector QE. Also included is the X-ray transmission of a 60 nm Al thermal filter on the input face of the microchannel plates, and an additional 100nm of Al on 300nm of polyimide as an optical filter directly in front of the focal plane array. The calculated Grasp at 1 keV is 0.032 cm^2 sr.

Let us consider a "focusing" collimator and planar collimator of equal aperture; a planar collimator would have a grasp of ~0.096 cm^2 sr, a factor of ~3 larger than MIXS-C, However, this requires a factor of 16 greater focal plane area, which is limited for MIXS (cooling power, cost, development time). Therefore, a planar collimator would be unsuitable for MIXS and the advantages of using a focusing collimator are clear.

The grasp, *G,* for an imaging telescope (MIXS-T) can be calculated from the on-axis effective area $A(0,E)$ and the vignetting function. For an instrument with a circular FOV the element $d\Omega$ of solid angle subtended by an angular element $d\xi$ at an off-axis angle ξ is approximated at small off-axis angles by

$$d\Omega = 2\pi\xi d\xi \qquad (2)$$

and the off-axis effective area $A(\xi,E)$ is

$$A(\xi, E) = A(0, E)V(\xi, E), \qquad (3)$$

The grasp $G(E)$ is given by

$$G(E) = 2\pi\varepsilon_d(E)T(E)A(0,E)\int_0^{\xi_{\max}}\xi V(\xi,E)d\xi, \qquad (4)$$

where $\varepsilon_d(E)$ is the detector QE and $T(E)$ is the combined transmission of the optical and thermal filters in front of the detectors.

An approximation to the vignetting function can be obtained by assuming that there is a linear fall off from the peak on-axis effective area to a minimum of zero at the edge of the field of view, which is defined by the 19.2 × 19.2 mm detector, which at a 1m focal length gives an FOV of 1.1° (0.55° half angle). Using this approximation for the vignetting function and assuming a perfect detector and 50cm^2 on axis effective area, G is estimated to be ~0.009 cm^2 sr. Figure 12 shows the MIXS-T grasp ($G(E)$), incorporating a more realistic vignetting function generated by Monte-Carlo raytracing software (Figure 11), the detector's QE and the calculated absorption of a 60 nm thick Al thermal filter on the input optic surface and a 100 nm Al optical filter deposited on 300nm of polyimide. The grasp is calculated for both focussed X-rays and for all rays incident in the focal plane, as shown in Figure 10,.

9 Instrument background levels and minimum detectable flux

The sensitivity of a photon-detecting instrument can be quantified by the minimum detectable flux I_{min}, which is the minimum signal flux from a source that can be distinguished from the background B. We assume that an isotropic flux I (in units of photons cm^{-2} s^{-1} sr^{1}) of fluorescent X-rays at a discrete energy (in keV) from an extended source is incident on the front of an instrument with a grasp G. This instrument has a focal plane detector with an area for photon detection A_{det} and energy resolution δE. The detected fluorescent X-ray signal is accompanied by a background of solar X-rays which are scattered from the surface under examination, denoted by I_{scat} (in units of photons cm^{-2} s^{-1} sr^{-1} keV^{-1}).

Although features in the scattered continuum may contain information on surface properties and absorption features in the continuum may yield compositional information, in terms of measuring fluorescence spectra the continuum constitutes a background and is treated as such here. The detector also has a non-X-ray background component, caused by charged particle events B_p (units of events cm^{-2} s^{-1} keV^{-1}). For a cooled, photon-counting detector, intrinsic thermal noise is negligible and the scattered X-ray component and the particle induced background will dominate. If a signal to noise ratio R is required for the detection of an X-ray line then I_{min} may be defined as the flux that, in a given integration time, produces a count R standard deviations of B above its mean. I_{min} for a given value of R (typically taken to be 3 -5) is given by

$$I_{\min} = \frac{R\sqrt{\delta E(B_p A_{\det} + I_{scat} G)}}{G\sqrt{t}}. \quad (5)$$

The particle-induced X-ray background B_p results from a combination of both high energy cosmic rays and lower energy (10-100 MeV) protons ejected from the Sun. To reduce B_p MIXS's detectors are shielded by 15 mm of Al, which is the Continuous Slowing Down Approximation (CSDA) range for 60 MeV protons in Al.

In the absence of direct measurements at Mercury, in order to calculate the expected instrument background, we must use data for the integrated intensities of solar X-rays and protons in various energy bands, measured in geostationary orbit at 1 AU by the Energetic Particle Sensor (EPS) on the GOES spacecraft (Sellers et al., 1996). EPS data show a poor correlation between the flux of protons with energies > 60 MeV and X-ray flux for most solar conditions, and for lower energy protons the flux can be highly variable. For high (M – X) X-ray flare states, however, the flux of > 60 MeV protons may increase by several orders of magnitude, with the peak in proton flux occurring some time after the X-ray flux. At 1 AU the time delay between the peaks in the X-ray and proton fluxes during an X-flare is typically of the order 2 hours. At Mercury the delay will be between approximately 35 and 55 minutes for perihelion and aphelion, respectively. The MIXS background count rates due to solar protons will typically vary by less than one order of magnitude for the majority of the instrument lifetime. Very large solar flares may however be followed, within an hour, by an increase in background of several orders of magnitude.

We have estimated the MIXS background at Mercury by scaling that experienced by the XMM Newton X-ray observatory's EPIC X-ray camera's pn-CCDs (Strüder et al., 2001) which are in a highly elliptical orbit around the Earth. These are analogous to the MIXS detectors and are considered useful for comparison with MIXS. . Cosmic ray and solar proton events in the EPIC pn detectors are rejected on the basis of energy, or the shapes of tracks left by particles as they deposit energy in adjacent pixels. The post-rejection background rate for the pn-CCDs is reported to be 0.039 cm^{-2} s^{-1} in the energy band 0-10 keV (Lumb, 2002) giving a count rate per keV of 0.0039 cm^{-2} s^{-1} keV^{-1}. XMM Newton's CCDs have 30mm Al shielding for the detectors which can be penetrated by particles with energies > 90 MeV. The fluxes for >90 MeV protons are typically a factor 2-3 less than for > 60 MeV protons (Xapsos, 2000). The proton flux at Mercury for all energies can be assumed to scale relative to that at 1 AU according to an inverse square law dependence on the distance from the Sun (Mukai, 2003).

The energy deposited by minimum ionising particles (MIPS) in a silicon X-ray detector is a function of the distance travelled in a single detector pixel and has been simulated by Strüder (2000) who shows that for a 150μm × 150μm × 300μm Si pixel the Landau energy distribution peaks at about 40 keV. This peak corresponds with a most probable distance travelled in a single pixel of 150μm. Scaling this distribution to account for the larger MIXS pixel size (300 × 300 × 450 μm) gives a peak at 80 keV and approximately 10% of energy deposited by MIPS will be in the energy band 0-10 keV. The MIXS energy band is from 0.5-7.5 keV. The distribution varies little over the range 0-10 keV and it is therefore assumed to be constant within this energy range. Consequently, a background rate in the 0.5-7.5 keV energy band of 0.04 cm^{-2} s^{-1} keV^{-1} is calculated.

If a three order of magnitude increase in flux is assumed after high flare states then the background rate may reach values of 40 cm^{-2} s^{-1} keV^{-1}. The background value given for the XMM-Newton detectors, however, includes galactic cosmic rays and solar protons and it is inappropriate to scale the former event rate with distance from the Sun. Solar protons are believed to contribute only ~10% of the XMM background at 1 AU on average (Strüder, 2000). If only 10% of the 1 AU background value attributable to SEPs is scaled to 0.31 AU then the typical MIXS background under normal conditions is estimated to be ~0.008 cm^{-2} s^{-1} keV^{-1}. We have therefore adopted 0.04 cm^{-2} s^{-1} keV^{-1} as a worst-case background rate.

10 The detection of elements by MIXS

Using Equation 7 we have calculated the time required for 3σ detection of the various elemental lines of interest in different solar flare states, for which the incident solar spectra are shown in Figure 2. It is assumed that a minimum of ten photons is required for a significant detection. The calculated integration times for MIXS-T and –C are shown in Table 3 and Table 4 respectively. A worst case value of 0.04 cm^{-2} s^{-1} keV^{-1} is assumed for the particle background B_p. The L shell emission lines of Ti and Cr are coincident with the far more intense O-K line and therefore cannot be separated and are not included here. Where the required integration times are longer than 1 year, an element is considered to be undetectable and is left blank in the tables. The spatial scales on which elements may be measured are defined by the required integration times, the instrument FOVs and by the orbital velocity of the BepiColombo MPO. The imaging capability of MIXS-T allows data to be manipulated for optimum imaging or spectroscopy. For MIXS-T it is assumed initially that all photons in the focal plane are added together and the imaging capability within the field of view is not applied, this optimises the measurement statistics for spectroscopy. For times where the flux from Mercury is high, the imaging capability of MIXS-T can be applied, by subdividing the focal plane into its imaging pixels, the application of imaging to various elements is discussed below.

The number of counts from single surface elements can be maximised by combining measurements made of the same surface area during multiple passes overhead (using the solar spectrum, as measured by SIXS to allow normalisation between subsequent orbits). The coverage time achieved as a function of position on the surface has been calculated using the Satellite Tool Kit (STK) (Analytical Graphics Inc.) for illuminated segments of the planet during one year of operations beginning in September 2019. The resultant coverage map for MIXS-T is shown in Figure 13 and for MIXS-C in Figure 14. The nodes used in the calculation are positioned on the surface at 4° latitude and longitude intervals. The structure visible in the images is a combination of the node spacing and the effect of including only dayside observations in the measurements. Typical accumulated coverage times for near-equatorial regions of approximately hundreds of seconds increase to more than three hundred seconds at high latitudes. For MIXS-C we calculate accumulated coverage times of ~9000 seconds in near-equatorial regions, increasing to almost 30000 seconds at high latitudes. Assuming a "worst case" scenario in which all measurements of a surface element are made during solar quiet, the number of counts expected for MIXS-T is shown in Table 5 and for MIXS-C is shown in Table 6, assuming nadir viewing and normal incidence for solar X-rays. A more typical scenario would see ~20% of the year in B-flare state during solar minimum (Huovelin et al., this volume). The percentage errors shown in the tables correspond to the Poissonian errors in the number of counts.

The dwell times for a surface element (the time between a point on the surface entering and then leaving the FOV) during single passes by MIXS-C at apoherm and periherm are, respectively, 209 and 27.9 seconds. For MIXS-T, the dwell times at apoherm and periherm are 22.1 and 3.0 seconds. Measurements made in a single surface element during solar flare events will contain many more counts than during solar quiet and provide access to X-ray lines with higher energies than can be measured during low solar flare states. Simulated spectra for single passes at apoherm (1500 km altitude) are shown for MIXS-T in Figure 15 and for MIXS-C in Figure 16. The spectra assume nadir pointing and normal incidence for solar X-rays at a Sun-Mercury distance of 0.39 AU. The detectors have 40 eV energy bins and, for illustrative purposes, the surface is assumed to have the lunar high-K basalt composition of Table 2. We assume a FWHM energy resolution of 100eV at 1 keV, varying as a function of energy according to Equation 3. In the period after an X-flare, the solar proton flux may (in extreme cases) increase by five orders of magnitude, implying a particle-induced background in the detector of 400 cm^{-2} s^{-1} keV^{-1}. If X-flare intensities are maintained in the period post flare then the sensitivity of the instrument to weaker K_{β} lines is reduced but does not alter the sensitivity to the more intense K_{α} lines shown here, other than for P-K_{α} which can no longer be detected. This is primarily because the background due to the scattered X-ray continuum is typically much greater than the proton-induced background. The enhanced proton flux following a flare can take several days to decay, while the X-ray flux returns to typical values within hours. During these periods, the proton background may remain sufficiently high relative to the X-ray signal that measurements may be compromised.

The imaging capability of MIXS-T allows measurements from surface areas smaller than the surface footprint of the 1.1° FOV. For M1 and X1 flares (assuming that the incident solar intensity for an X1 flare = 10 M1), Table 8 gives an estimated spatial resolution achievable from apoherm for key elements which still give a statistically significant measurement as described in Section 5 and summarised in Table 7. A maximum resolution of 2 arc minutes is reported in the table as this is the goal of the MIXS-T optics, although the formal requirement is for an angular resolution of less than 9 arc minutes. The grasp values for focussed rays only are used in these calculations.

Global abundance averages for elements may be measured by integrating spectra accumulated during the entire mission. Table 9 shows the total number of counts in major elemental lines expected for MIXS-C in one year, assuming a worst case scenario in which all measurements are made during solar quiet and assuming measurements are made at 0.39 AU. A mean angle for incident solar X-rays of 45° is assumed and only dayside measurements are considered.

However, unless Mercury has only one widespread type of crust, combining measurements to give global averages may obscure important variations and result in geologically uninformative results. Because of the divergent formation mechanisms for primary and secondary crust (Section 4), it will be more useful to make separate calculations of average element abundances in primary and secondary crust. To separate the two sets of measurements, we will use data from other BepiColombo experiments (notably SIMBIO-SYS and MERTIS) to help to map the extent of each crustal type.

10.1 Validation of the fluorescence model

To validate our X-ray spectral calculations, we compare X-ray spectra of the Moon, made by the Chandra X-ray observatory ACIS instrument and presented by Wargelin et al. (2004), with synthetic spectra generated using the fluorescence model presented above.

The Chandra observations were made in July 2001 using the I2 and I3 front illuminated chips of the Advanced CCD for Imaging Spectroscopy (ACIS) focal plane instrument (Garmire et al, 2003).

The GOES X-ray data sets for the period of the Chandra observations of the Moon typically show a mid B-flare state. In the following simulations, a B2 flare state is modelled as a B1 flare, as in Figure 2, multiplied by two, independent of energy. The composition of the large areas of the lunar surface observed by Chandra is unknown; the modelled spectra represent the two possible lunar soil compositions given by Clark and Trombka (1997); Apollo 16 Highlands and Apollo 12 mare basalt. The calculations assume that the illuminated lunar surface is perfectly smooth. The illumination angle θ and the observation angle ϕ are taken to be 45°, approximating the geometry illustrated by Wargelin et al. (2004). The I2 and I3 effective area as a function of energy for the ACIS-I instrument was determined from the Chandra Science Data Center (http://asc.harvard.edu/proposer/POG/). The FWHM energy resolution of the measured spectrum presented by Wargelin et al., (2004) is ~111 eV at the O-K line (0.525 keV) and is scaled to other energies here according to Equation 3. The aperture of a single ACIS-I CCD is 5.9×10^{-6} steradians and the combined I2 and I3 integration time is 8063 s (Wargelin et al, 2004). The simulated spectra are shown in Figure 17 along with the measured peak count rates for O-K, Fe-L and Si-K.. There is good agreement between measurement and model; in particular, this comparison demonstrates the feasibility of detecting iron in planetary regoliths at all solar states via the L-shell emission.

The correct interpretation of X-ray measurements from the surface of Mercury will require a detailed understanding of the processes that generate X-rays and the effects of observing a real planetary surface as opposed to an idealised surface as modelled herein. Theoretical and experimental investigations are proceeding to investigate the effects of surface and regolith properties on emission spectra. Investigations are also ongoing into the likely properties of the Mercurian magnetosphere and the X-ray emission that may result from its interaction with the surface and exosphere as well as the solar wind. The results of these investigations will be reported in future papers.

11 MIXS at Mercury

By accumulating data globally and/or for regions representing primary and secondary crust, we expect to be able to measure at least Na, Mg, Al, Si, P, K, Ca, Ti, Fe and Ni (although separation of the Ni-L line from the much more intense O-K line may prove challenging), all to a high statistical precision. These data can be subdivided into data from the various, large scale, Mercurian terrains. If Mercury has exposed primary crust as well as secondary crust, subsets of data, representing areas dominated by primary crust and areas dominated by secondary crust, will be more informative than global averages.

Under typical solar conditions MIXS-T will determine Na, Mg, Al, Si and Fe abundances on scales of some tens of km, and MIXS-C will achieve scales of hundreds of km with greater numbers of counts to provide increased statistical certainty for the spectral lines. During solar flares, MIXS-C will have the capability to measure P, K, Ca, Ti, Cr, while Na, Mg, Al, Si and Fe will be measured with increased statistical certainty. Spatial scales of hundreds of km are sufficient to subdivide the surface of Mercury into the individual terrains identified on Mariner-10 images; for example heavily cratered terrain and intercrater plains (possibly both primary crust), smooth plains (probably secondary crust) and 'hilly and lineated terrain' and 'hummocky plains' (probably impact-modified versions of other terrain units) (e.g. Trask and Guest, 1975; Strom, 1997; Strom and Sprague, 2003). It may be possible to distinguish differences in composition between individual lava flows in compound flow fields to indicate the fractionation history of magma chambers or the time-related depth of magma sources.

Highest spatial resolution measurements of just a few km will be achieved by MIXS-T during solar flares for the major elements Na, Mg, Al, Si, P, K, Ca, Ti, Fe. These measurements will provide access to a wide range of landforms including possible volcanic constructs, craters of various diameters and depths as well as their central peaks. The latter are uplifted material from the middle or lower crust and so may expose strata formed during various eras in Mercury's history (including primary crust, which will be important if it is not widespread at the surface) and/or bodies of magma intruded into the crust. The youngest craters and their ejecta may also provide information on the rate and nature of space weathering.

MIXS observations of X-ray emission from Mercury will allow the determination of elemental abundances with unprecedented spatial resolution for a range of elements of key importance for understanding the geology, evolution and formation of the planet. X-ray emission will also provide a mechanism for investigating the unique surface-magnetosphere interactions at Mercury.

Since preparation of this paper, the Messenger flyby data from the Gamma-ray spectrometer has been able to place a 0.5 wt % upper limit on the potassium content of the equatorial regions of Mercury. This is shown to rule out formation models which include k-rich feldspar. Future observations of this kind will be used to inform and improve the performance predictions for MIXS at Mercury. To date, a number of assumptions about the nature of the planet's surface have been made which were constrained only by our knowledge of the properties of the regolith and the superficial resemblance of Mercury to the Moon.

12 Acknowledgements

We thank the European Space Agency's BepiColombo team and Peter Nieminen of ESA for providing a detailed description of the polynomial approximations to Solar X-ray spectra. MIXS is supported by the Science and Technology Facilities Council (STFC) in the UK, TEKES in Finland, The Max Planck Society in Germany and INTA in Spain.

13 References

Adler, I and Trombka, J.I., 1970. Geochemical exploration of the Moon and planets, Springer-Verlag, New York.

Adler, I., Gerard, J., Trombka, J., Lowman, P., Blodgett, H., Yin, L., Eller, E., Lamothe, R., 1972. The Apollo 15 X-ray fluorescence experiment, Proc. Lunar Sci. Conf. 3rd, 3, 2157-2158.

Adler, I., Trombka, J. I.., Schmadebeck, R., Lowman, P., Blodget, H., et al., 1973. Proceedings of the Lunar Science Conference, 4, 2783.

Ashenbach, 1985. X-ray telescopes, Rep. Prog. Phys., 48, 579-629.

Basaltic Volcanism Study Project, Basaltic volcanism on the terrestrial planets, 1981. sponsored by the Lunar and Planetary Institute, Pergamon Press, New York, 1286 pp.

Benz, W, Slattery, W.L., Cameron, A.G.W., 1988, Collisional stripping of Mercury's mantle, Icarus, 74, 516-528.

Benz, W., Anic, A., Horner, J., Whitby, J.A., 2007, The origin of Mercury, Space Science Reviews, DOI 10.1007/s11214-007-9284-1.

Bland, P. A. and Benedix, G. K., 2006. Volatile depletion: Constraints from differentiated meteorites. Meteoritics & Planetary Science 41, A22-A22.

Blewett, D. T., Hawke, B. R., Lucey, P. G., 2002, Lunar pure anorthosite as a spectral analog for Mercury, Meteoritics and Planetary Science, 37, 1245-1254.

Brodrick, D., S. Tingay, and M. Wieringa, 2005. X-ray magnitude of the 4 November 2003 solar flare inferred from the ionospheric attenuation of the galactic radio background, J. Geophys. Res., 110, A09S36, doi:10.1029/2004JA010960.

Burbine, T. H., Trombka, J. L., Bergstrom Jr., P.M. and Christon, S.P., 2005, Calculating the X-ray Fluorescence from the Planet Mercury due to High Energy Electrons, LPSC XXXVI, no. 1415.

Cameron, A.G.W., 1985, The partial volatilization of Mercury, Icarus, 71, 337-349.

Cameron, A.G.W., Fegley, B., Benz, W. and Slattery, W.L., 1988. The Strange Density of Mercury: Theoretical Considerations, In Mercury, Eds. M.S. Matthews, C. Chapman and F. Vilas, University of Arizona Press, Tucson, 692 – 708.

Clark, P.E., S.R. Floyd and J.E. Trombka, 1997. The Effectiveness of the Proportional Counter as a Solar X-Ray Monitor for the NEAR Mission, Conference on the High Energy Radiation Background in Space, Workshop record, 90.

Clark, P.E. and J.I. Trombka, 1997. Remote X-ray fluorescence experiments for future missions to Mercury. Planet. Space. Sci, 45, 57-65.

Fichtel, C.E. and J.I. Trombka, 1997. Gamma Ray Astrophysics, New insight to the Universe, 2nd Edition, NASA Ref. Publ., 1386.

Fraser, G.W., 1989. X-ray detectors in Astronomy, Cambridge University Press.

Fraser, G.W., A.N. Brunton, J.E. Lees, J .F. Pearson and W.B. Feller, 1993. X-ray focusing using square-pore microchannel plates: First observation of cruxiform image structure Nuc. Ins. and Meth. A324, 404-407.

Fegley, B. and Cameron, A.G.W., 1987. A vaporization model for iron/silicate fractionation in the Mercury protoplanet, Earth and Planetary Science Letters, 82, 207-222.

Garmire, G.P., Bautz, M.W., Ford, P.G., Nousek, J.A., Ricker, G.R., Jr., 2003, Advanced CCD imaging spectrometer (ACIS) instrument on the Chandra X-ray Observatory, Tananbaum. *Proc. SPIE*, 4851, 28-44.

Goettel, K.A., 1988. Present bounds on the bulk composition of Mercury - Implications for planetary formation processes, In Mercury, Eds. M.S. Matthews, C. Chapman and F. Vilas, Tucson, AZ, University of Arizona Press, 613-621.

Grande, M., 1997. Investigation of magnetospheric interactions with the Hermean surface, Adv. Space. Res., 19, 1609-1614.

Grande, M., Browning, R., Waltham, N., Parker, D., Dunkin, S. K. et al., 2003. The D-CIXS X-ray mapping spectrometer on SMART-1, Planetary and Space Science, 51, 427-433.

Grande, M., Maddison, B.J., Sreekumar, P., Huovelin, J., Kellet, B.J., Howe, C.J., Crawford, I., Holland, A., and the CIXS team, 2008. The C1XS X-ray spectrometer on Chandayaan 1. LPSC XXXIX, Abstract #1620.

Huovelin, J., Grande, M., Vainio, R., Malkki, A., Alha, L., Fraser, G.W., Kato, M., Koskinen, H., Muinonen, K., Naranen, J., Schmidt , W., Syrjasuo, M., Anttila, M., Vihavainen, T., Andersson, H., Kiuru, E., Roos, M., Valtonen, E., Peltonen, J., Talvioja, M., Portin, P., Prydderch, M., 2008. Solar Intensity X-ray and particle Spectrometer (SIXS), Planetary and Space Science, Present Volume.

Huovelin, J., Alha, L., Andersson, H., Andersson, T., Browning, R., Drummond, D., Foing, B., Grande, M., Hämäläinen, K., Laukkanen, J., Lämsä, V., Muinonen, K., Murray, M., Nenonen, S., Salminen, A., Sipilä, H., Taylor, I., Vilhu, O., Waltham, N., Lopez-Jorkama, M., 2002. The SMART-1 X-ray solar monitor (XSM): calibrations for D-CIXS and independent coronal science, Planetary and Space Science, 50, 1345-1353.

Jefimovs, K., Vila-Comamala, J., Pilvi, T., Raabe, J. Ritala, M and David. C., 2007. Zone-Doubling Technique to Produce Ultrahigh-Resolution X-Ray Optics, Physical Review Letters, 99, 264801.

Jeanloz, R., Mitchell, D. L., Sprague, A. L., de Pater, I., 1995. Evidence for a basalt-free surface on Mercury and implications for internal heat, Science, 268, 1455-145.

Leary, J. C., Conde, R. F., Dakermanji, G., Engelbrecht, C. S., Ercol, C. J., Fielhauer, K. B., Grant, D. G., Hartka, T. J., Hill, T. A., Jaskulek, S. E., Mirantes, M. A., Mosher, L. E., Paul, M. V., Persons, D. F., Rodberg, E. H., Srinivasan, D. K., Vaughan, R. M., Wiley, S. R., 2007, The MESSENGER spacecraft, Space Science Reviews, 131, 187-217.

Lowe, B.G., Holland, A.D., Hutchinson, I.B., Burt, D.J. and Pool, P.J., 2001. The swept charge device, a novel CCD based EDZ detector: first results, Nucl. Inst. Meth. A, 458: 568-579.

Lumb, D., 2002. EPIC in orbit background, Proc. New Visions of the X-ray Universe in the XMM-Newton and Chandra Era, ESA SP-488.

Margot, J.L., Peale, S.J., Jurgens, R.F., Slade, M.A., and Holin, I.V., 2007. Large longitude libration of Mercury reveals a molten core, Science, 316, 710-714.

Milillo, A., Wurz, P., Orsini, S., Delcourt, D., Kallio, E., Killen, R.M., Lammer, H., Massetti, S., Mura, A., Barabash, S., Cremonese, G., Daglis, I.A., De Angelis, E., Di Lellis, A.M., Livi, S., Mangano, V. and Torkar, K, 2005. Surface-Exosphere-Magnetosphere System Of Mercury, Space Sci. Rev., 117, 397–443.

Morgan, J.W. and Anders, E., 1980. Chemical composition of earth, Venus, and Mercury, Proc. Natl. Acad. Sci. USA, 77, 6973-6977.

Mukai, T., K. Ogasawara and Y. Saito, 2003. An empirical model of the plasma environment around Mercury, Advances in Space research, 33, 2166-2171.

Ness, N.F., 1979. The Magnetosphere of Mercury, in Solar System Plasma Physics, vol. II, Eds. C.F. Kennel, L.J. Lanzerotti and E.N. Parker, North-Holland, New York, 185–206.

Näränen, J., Parviainen, H., Muinonen, K., Nygard, K., Peura, M. and Carpenter, J.D., 2008. Laboratory studies into the effect of regolith on planetary X-ray fluorescence spectroscopy, Icarus, under review.

Näränen, J., Parvianen, H. and Muinonen, K., 2007. X-ray fluoresence modelling for solar system regoliths: effect of viewing geometry, particle size, and surface roughness, Proceedngs of the 236th IAU Symposium: Near Earth objects, Our Celestial Neighbours: Opportunities and Risk, Cambridge University Press. doi:10.1017/S1743921307003298.

Okada, T., Particle Size Effect in X-Ray Fluorescence at a Large Phase Angle: Importance on Elemental Analysis of Asteroid Eros (433). Lunar Planetary Sci., 35, 1927, 2004.

Okada, T., Shirai, K., Yamamoto, Y., Arai, T., Ogawa, K. et al., 2006. X-ray Fluorescence Spectrometry of Asteroid Itokawa by Hayabusa, Science, 312,. 1338-1341.

Price, G.J., A.N. Brunton,, M.W. Beijersbergen, G.W. Fraser, M. Bavdaz, J.-P. Boutot, R. Fairbend, S.-O. Flyckt, A. Peacock, E. Tomaselli, 2002. X-ray focusing with Wolter microchannel plate optics, Nuc. Ins. and Meth., A 490, 276–289.

Robinson, M. S., Taylor, G. J., 2001. Ferrous oxide in Mercury's crust and mantle, Meteoritics and Planetary Science 36, 841-847.

Russell, C.T., Baker, D.N. and Slavin, J.A., 1988. The Magnetosphere of Mercury, in Mercury, Eds. F. Vilas, C.R. Chapman and M.S. Matthews, University of Arizona Press, Tucscon, 514–561.

Schlemm C.E, Starr, R. D., Ho, G.C., Bechtold, K.E., Hamilton, S.A., Boldt, J.D., Boynton, W.V., Bradley, W., Fraeman, M.E., Gold, R.E., Goldsten, J.O., Hayes J.R., Jaskulek, S.E., Rossano, E., Rumpf, R.A., Schaeferm, E.D., Strohbehn, K., Shelton, R.G., Thompson, R.E., Trombka J.I., Williams, B.D., 2007. The X-Ray Spectrometer on the MESSENGER Spacecraft, Space Sci Rev, 131, 393-415.

Sellers, F.B. and Hanser, F.A., 1996. Design and calibration of the GOES-8 particle sensors: the EPS and HEPAD, Proc. SPIE 2812, 353-364.

Shirai, K., Okada, T., Yamamoto, Y., Arai, T., Ogawa, K., Shiraishi, H., Iwasaki, M., Arakawa, M., Grande, M, Kato, M., 2008, Instrumentation and performance evaluation of the XRS on SELENE orbiter. Earth Planets Space, 60, 277-281, 2008

Slavin, J.A., 2004. Mercury's Magnetosphere, Adv. Space Res., 33, 1859–1874.

Solomon, S.C., 2003. Mercury: the enigmatic innermost planet, Earth and Planetary Science Letters, 216, 441-455.

Sprague, A. L., Hunten, D.M. and Lodders, K., 1995. Sulfur at Mercury, elemental at the poles and sulfides in the regolith. Icarus, 118, 211–215.

Sprague, A. L., Hunten, D.M. and Lodders, K., 1996. Erratum. Icarus, 123, 247.

Strom, R.G., 1997. Mercury: an overview, Advances in Space Research, 19, 1471-1485.

Strom, G. and Sprague, A.L., 2003. Exploring Mercury: The Iron Planet, Springer Praxis, New York.

Strüder, L., High resolution X-ray imaging X-ray Spectrometers, 2000. Nuc. Inst. Meth. A, 454, 73-113.

Strüder, L., Briel, U., Dennerl, K. and 55 other authors, 2001, The European Photon Imaging Camera on XMM-Newton: The pn-CCD camera, Astronomy and Astrophysics, 365, L18-L26.

Taylor, S. R., 1975. Lunar Science: A post-Apollo view, New York, Pergamon Press, Inc.

Taylor, S. R., 1989, Growth of planetary crusts, Tectonophysics, 161, 147-156.

Taylor, G. J. and Scott, E. R. D., 2004. Mercury, in Treatise in Geochemistry, Vol. 1. Meteorites, Comets, and Planets, Davis, A. M. (ed), Elsevier, 477-486.

Trask, N. J., Guest, J. E., 1975. Preliminary geologic terrain map of Mercury, Journal of Geophyscial Research, 80, 2461-2477.

Treis, J., Andricek, L., Herrmann, S., Heinzinger, K., Lauf, T., Lechner, P., Lutz, G., Mas-Hesse, J.M., Porro, M., Richter, R.H., Schaller, G., Schnecke, M., Schopper, F., Segneri, G., Soltau, H., Stevenson, T., Strüder, L., Whitford, C.W., Wölfel, S., 2008. DEPFET Based Focal Plane Instrumentation for X-ray Imaging Spectroscopy in Space; 2007 IEEE NSS conference record, IEEE Catalog Number 07CH37869C, N47-3.

Treis, J., Fischer, P., Hälker, O., Harter, M., Herrmann, S., Kohrs, R., Krüger, H., Lechner, P., Lutz, G., Peric, I., Porro, M., Richter, R. H., Strüder, L., Trimpl, M., Wermes, N., 2006, Study of noise and spectroscopic performance of DEPMOSFET matrix prototypes for XEUS, Nucl. Inst. Meth. A, 568, 1, 191-200.

Trombka, J.I., Squyres, S.W., Brückner, J., Boynton, W.V. Reedy, R.C. et al. 2000. The Elemental Composition of Asteroid 433 Eros: Results of the NEAR-Shoemaker X-ray Spectrometer, Science, 289. 2101 – 2105.

Truscott, P., Dyer, C. and Peerless, C., 2000. Basalt X-ray fluorescence study, DERA report, DERA/CIS/CIS2/7/36/4/1/3.

Tucker W.H. and M. Koren, 1971. Radiation from a high-temperature low-density plasma: the X-Ray spectrum of the solar corona, The Astrophysical Journal, 168, 283.

Wargelin, B.J., Markevitch, M., Juda, M., Kharchenko, V., Edgar, R., and Dalgarno, A., 2004, Chandra observations of the "dark" Moon and geocoronal solar wind transfer, The Astrophysical Journal, 607, 596–610.

Weidenschilling, S.J., 1978, Iron/silicate fractionation and the origin of Mercury, Icarus, 35, 99-111.

Willingale, R., Fraser, G.W., Brunton, A.N. and Martin, A.P., 1998. Hard X-ray imaging with microchannel plate optics, Experimental Astronomy. 8, 281-296.

Xapsos, M.A., Summers, G.P., Barth, J.L., Stassinopoulos, E.G. and Burke, E.A., 2000. Probability Model for Cumulative Solar Proton Event Fluences, IEEE Trans. Nucl. Sci., 47, 486-490.

Zhang, C., Lechner, P., Lutz, G., Porro, M., Richter, R., Treis, J., Strüder, L. Nan Zhang, S., 2006. Development of DEPFET Macropixel detectors, Nucl. Inst. Meth. A, 568, 1, 207-216.

Zombeck, M.V., 2007. Handbook of Space Astronomy and Astrophysics, Third Edition, Cambridge University Press.

Figure 1. A Schematic illustration of MIXS showing the adjacent MIXS-T and MIXS-C channels.

Figure 2. Polynomial approximations to the solar X-ray spectrum in M1, C1 and B1 flare states derived from various sources as described in the text together with measured solar X-ray spectra from the X-ray Solar Monitor (XSM) instrument on SMART 1. Also shown is the predicted magnitude of the diffuse X-ray background (DXB) measured by XSM between 3 keV and 7 keV.

Figure 3. Simulated fluorescence emission spectrum from a lunar basalt surface at 0.39 AU, under various solar flare conditions calculated using Equation 1. Lines are shown with a 2 eV width.

Figure 4. Scanning electron microscope image showing the Ir coated, square microchannel structure of an MCP X-ray optic.

Figure 5. Calculated quantum efficiency of the MIXS FPA detectors.

Figure 6. Geometry of the MIXS-C slumped collimator. The side length of the collimator is 80mm and the 550 mm separation of the MCP collimator and the detector is equal to the collimator's spherical slump radius. The acceptance half angle for a single channel is defined by its aspect ratio (L:d).

Figure 7. Raytraced effective area as a function of off axis angle for the Ir coated MIXS-C optics at 1 keV.

Figure 8. Illustration of the path of an X-ray through sections of the front and rear slumped MCP optic microchannels, which together are a conical approximation to a true Wolter type I optic. The three channel lengths shown correspond to the inner, middle and outer rings of the MIXS-T optic.

The channel side length in each case is 20µm and the thickness of the septal wall between microchannels is 6 µm.

Figure 9. Schematic diagram of the MIXS-T MCP Wolter optics in cross section (not to scale). The front MCPs are slumped to a radius of 4m. The rear MCPs are slumped to a radius of 1.33 m. The mosaics of MCPs are arranged in three rings of differing thicknesses which approximate an ideal 1/r profile in channel thickness (see text). Rays are reflected from the internal surfaces of both front and rear microchannels and are focussed at a distance of 1m from the optic. The MIXS-T optic as viewed from the front and showing the arrangement of the sectors and rings is shown in Figure 1. The middle section in the pattern does not contain an MCP optic – this area is masked by the telescope structure.

Figure 10. On-axis effective area for the MIXS-T MCP optics. Focused rays are those that arrive at the focus of the telescope. The focus of the telescope is defined by the FWHM of the peak generated on a detector by parallel rays entering the aperture, the effective area is calculated for all rays that are truly focused by the optics (one reflection in each MCP). Focal plane in the figure refers to all rays arriving in the focal plane, including non-focussed rays that have been scattered or undergone multiple reflections in the optics.

Figure 11. The reduction in effective area with off axis incident angle, relative to the on-axis value (vignetting) for MIXS-T at four different X-ray energies.

Figure 12. Grasp G as a function of energy for MIXS-T and MIXS-C. The structure indicated is the result of X-ray absorption by the Ir coating.

Figure 13. Hammer-Aitoff projection of Mercury showing the predicted day side coverage time as a function of latitude and longitude on Mercury for MIXS-T during one year of operations beginning in September 2019. Craters shown are major craters observed by Mariner 10.

Figure 14. Hammer-Aitoff projection of Mercury showing the predicted day side coverage time as a function of latitude and longitude on Mercury for MIXS-C during one year of operations beginning in September 2019. Craters shown are major craters observed by Mariner 10.

Figure 15. Simulated X-ray spectra for MIXS-T during a single 22.1 s pass at apoherm in various solar flare states and assuming normal solar illumination and a nadir viewing angle at 0.39 AU. The spectra have 100 eV FWHM energy resolution at 1keV and the bin width is 40 eV.

Figure 16. Simulated X-ray spectra for MIXS-C during a single 209 s pass at apoherm in various solar flare states and assuming normal solar illumination and a nadir viewing angle at 0.39 AU. The spectra have 100 eV FWHM energy resolution at 1keV and the bin width is 40 eV.

Figure 17. Simulated Chandra ACIS X-ray spectra of the Moon for highland and Mare lunar soil compositions. Also shown are peak values for the Chandra ACIS lunar X-ray spectrum presented by Wargelin et al. (2004). The energy bin width shown here is 30 eV.

Table 1 Percentage by mass of some major elements in Mercury's bulk silicate fraction for nine models of Mercury's formation, [1]Morgan and Anders, 1980; [2]Chapter 4, Basaltic Volcanism on the Terrestrial Planets, 1980; [3] models 3 of 4 of Fegley and Cameron, 1987; [4]Goettel, 1988).

Table 2. Compositions of rocks (% by mass for the main elements) in the lunar crust, to give an indication of the possible variability of composition that might be encountered during study of Mercury's crust. Also shown are the line energies for X-rays in the MIXS 0.5-7.5 keV energy band. The compositional data is derived from % mass oxides data from Taylor (1975). The mass fraction not shown is O.

Table 3. Integration times in seconds required for MIXS-T to detect various elements in different solar flare states assuming a high K lunar basalt surface composition.

Table 4. Integration times in seconds required for MIXS-C to detect various elements in different solar flare states assuming a high K lunar basalt surface composition.

Table 5. Counts detected by MIXS-T in 100s during solar quiet.

Table 6. Counts detected by MIXS-C in 9000 s during solar quiet.

Table 7. The minimum precision required to allow for significant interpretation of measurements for possible minimum % mass values of various elements at Mercury. The table condenses the requirements from Section 5. A failure to meet one of these requirements does not necessarily detract significantly from the science as other elemental measurements may be sufficient. The % mass values are speculative minima based primarily on measurements of lunar rocks.

Table 8. Estimated spatial resolution achievable by MIXS-T in M1 and X1 flares to make "useful scientific measurements" as defined in Table 7.

Table 9. Predicted number of counts for major elemental lines detected by MIXS-C in 1 year of operations.

	Element % mass						
Model	**Na**	**Mg**	**Al**	**Si**	**Ca**	**Ti**	**Fe**
Chondritic formation[1]	0.03	20	3.4	22	3.7	0.2	5.8
Equilibrium condensation (EC)[2]		24	5.1	19	6.1	0.29	0.078
EC with usage of feeding zones[2]		25	3.8	21	4.7	0.22	0.06
Dynamically mixed[2]		29	2.5	20	2.9	0	0
Collisionally differentiated[2]		33	0	20	1.3	0	0
Vapourisation[3]		25	9	12	4.1	0.5	0.62
Refractory-rich[4]	0	21	8.8	15	11	0.43	0
Intermediate prefered[4]	0.074 - 0.37	19 - 22.9	1.9 - 3.7	16 - 22.4	2.5-5.0	0.090 - 0.18	0.78 - 7.8
Volatile-rich[4]	0.5	19	1.7	21	2.2	0.084	23.4

Table 1

1228 **Table 2:**

Element	X-ray Energies and emission lines(keV)	Anorthosite	Troctolite	Low-K Fra Mauro basalt	Medium-K Fra Mauro basalt	Apollo 15 green glass	Apollo 15 Quartz basalt	High-K Apollo 11 basalt
Si	1.74 (K)	20.7	20.5	21.8	22.5	21.4	22.9	19.0
Ti	4.51 (K)	0.04	0.10	0.7	1.3	0.17	0.9	7.1
Al	1.49 (K)	18.6	12.0	10.0	9.3	4.04	4.9	4.6
Fe	0.71 (L) 6.40 (Kα) 7.07 (Kβ)	0.52	3.81	7.5	8.5	15.3	14.5	14.8
Mn	5.91 (K)	0	0.05	0.0	0.0	0.16	0.2	0.2
Mg	1.25 (K)	0.48	8.86	6.6	5.2	10.0	5.7	4.6
Ca	3.70(Kα) 4.02(Kβ)	13.4	9.36	8.3	7.6	6.23	7.7	7.3
Na	1.04 (K)	0.59	0.29	0.3	0.5	0.09	0.2	0.4
K	3.35 (K)	0	0.00	0.2	0.7	0.03	0.0	0.4
P	2.02 (K)	0	0.00	0.0	0.0	0.00	0.0	0.1
Cr	5.41 (Kα) 5.95 (Kβ)	0	0.07	0.2	0.1	0.34	0.5	0.3
Ni	7.47 (Kα)	0	0.03	0.2	0.37		0.01	0.002

1229
1230

Table 3:

Element	**Line**	**Quiet Sun**	**B1 Flare**	**C1 Flare**	**M1 Flare**
O	K	0.04	0.05	0.08	0.007
Na	K	66	64	20	2.0
Mg	K	14	8.2	1.9	0.23
Al	K	58	17	3.2	0.42
Si	K	53	7.2	1.1	0.16
P	K	2.1×10^{7}	1.1×10^{5}	2000	170
K	K		2.5×10^{5}	270	61
Ca	Kα	3.2×10^{6}	3900	18	4.3
Ca	Kβ		2.3×10^{5}	140	32
Ti	Kα		2.57×10^{5}	58	12
Ti	Kβ		1.55×10^{7}	440	93
Cr	Kα			4.3×10^{4}	980
Cr	Kβ			2.3×10^{6}	6.1×10^{4}
Fe	Kα		1.5×10^{7}	440	40
Fe	Kβ			2.2×10^{4}	300
Fe	Lα	0.46	0.68	0.51	0.05
Fe	Lβ	0.50	0.74	0.53	0.05
Ni	Lα	3.9×10^{5}	5.0×10^{5}	1.9×10^{5}	1.8×10^{4}
Ni	Lβ	4.3×10^{5}	5.5×10^{5}	2.0×10^{5}	1.9×10^{4}

Table 4:

Element	**Line**	**Quiet Sun**	**B1 Flare**	**C1 Flare**	**M1 Flare**
O	K	0.01	0.01	0.02	0.0018
Na	K	13	12	3.8	0.42
Mg	K	2.7	1.53	0.36	0.04
Al	K	10	3.05	0.57	0.07
Si	K	8.4	1.15	0.17	0.03
P	K	$1.3x10^5$	960	80	13
K	K	$1.9x10^6$	1600	21	4.8
Ca	Kα	$1.5x10^4$	110	1.2	0.29
Ca	Kβ	$7.1x10^5$	900	8.5	2.0
Ti	Kα	$1.8x10^5$	750	3.1	0.66
Ti	Kβ	$8.1x10^6$	$3.4x10^4$	21	4.4
Cr	Kα		$5.1x10^6$	200	29
Cr	Kβ			3700	200
Fe	Kα	$2.6x10^6$	$1.5x10^4$	14	1.3
Fe	Kβ		$7.2x10^5$	95	8.6
Fe	Lα	0.09	0.13	0.09	0.01
Fe	Lβ	0.10	0.14	0.10	0.01
Ni	Kα				$1.2x10^6$
Ni	Lα	$6.6x10^4$	$8.2x10^4$	$3.3x10^4$	3400
Ni	Lβ	$7.2x10^4$	$8.9x10^4$	$3.4x10^4$	3600

Table 5:

Element	Line	Number of counts	% error
O	K	$1.3x10^4$	0.6
Na	K	14	30
Mg	K	70	10
Al	K	17	20
Si	K	19	20
Fe	Lα	1500	2
Fe	Lβ	1500	2

Table 6:

Element	**Line**	**Number of counts**	**% error**
O	K	6.1×10^{6}	0.03
Na	K	6500	1
Mg	K	3.4×10^{4}	0.5
Al	K	8700	1
Si	K	1.1×10^{4}	1
Fe	Lα	7.6×10^{5}	0.1
Fe	Lβ	6.6×10^{5}	0.1

Table 7:

Element	Possible minimum % mass	Minimum Precision required (%)
Si	20	5
Ti	1	20
Al	1	20
Fe	2	50
Mg	2	25
Ca	18	20
Na	0.4	Detection
K	0.1	Detection
Cr	0.05	Detection
Ni	0.04	Detection
S	0.1 (at poles)	Detection

Table 8:

Flare State	**X1**	**M1**
Element	Spatial resolution (km)	Spatial resolution (km)
Na	3	9
Mg	1	4
Al	2	6
Si	5	15
P	25	
K	15	
Ca	6	20
Ti	10	
Fe	1	1

1242 Table 9:

Element	Line	Counts	error (%)
O	K	$7.6x10^9$	0.00081
Na	K	$8.0x10^6$	0.034
Mg	K	$4.2x10^7$	0.015
Al	K	$1.1x10^7$	0.031
Si	K	$1.3x10^7$	0.027
P	K	12000	0.91
K	K	3200	1.77
Ca	Kα	37000	0.52
Ca	Kβ	5400	1.38
Ti	Kα	10000	0.96
Fe	Kα	3000	1.8
Fe	Lα	$9.0x10^8$	0.0028
Fe	Lβ	$5.7x10^8$	0.0029
Ni	Lα	98000	0.32
Ni	Lβ	90000	0.33

1243
1244

Figure 1

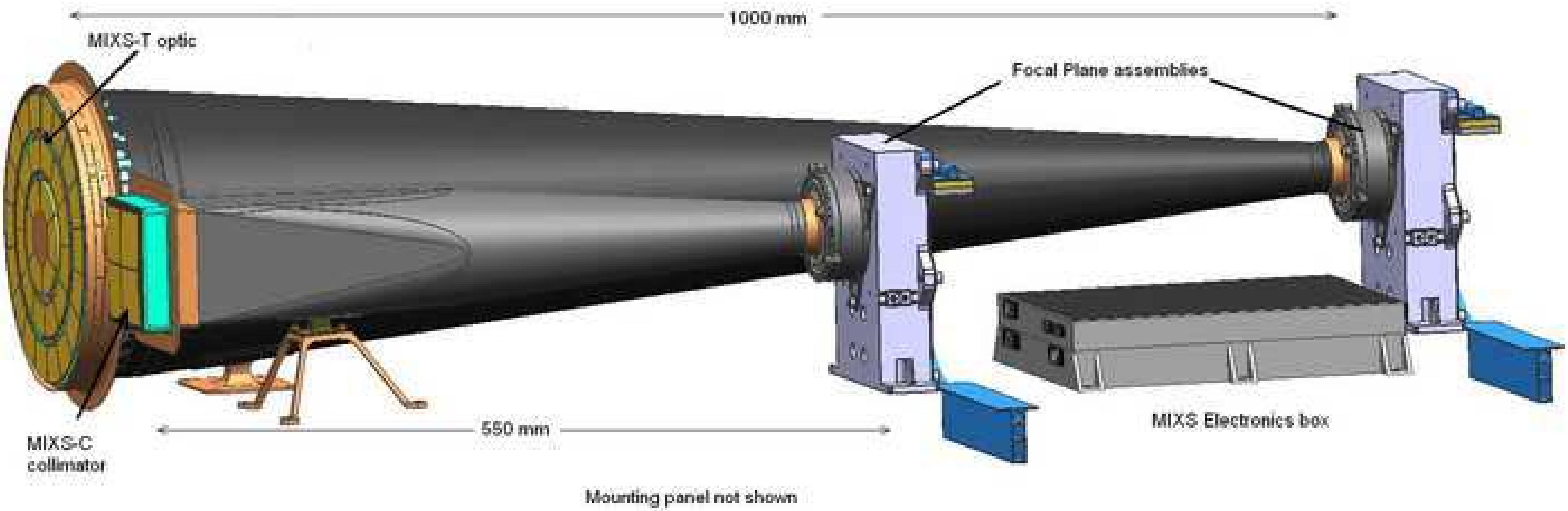
1000 mm
MIXS-T optic
Focal Plane assemblies
MIXS-C
collimator
550 mm
MIXS Electronics box
Mounting panel not shown

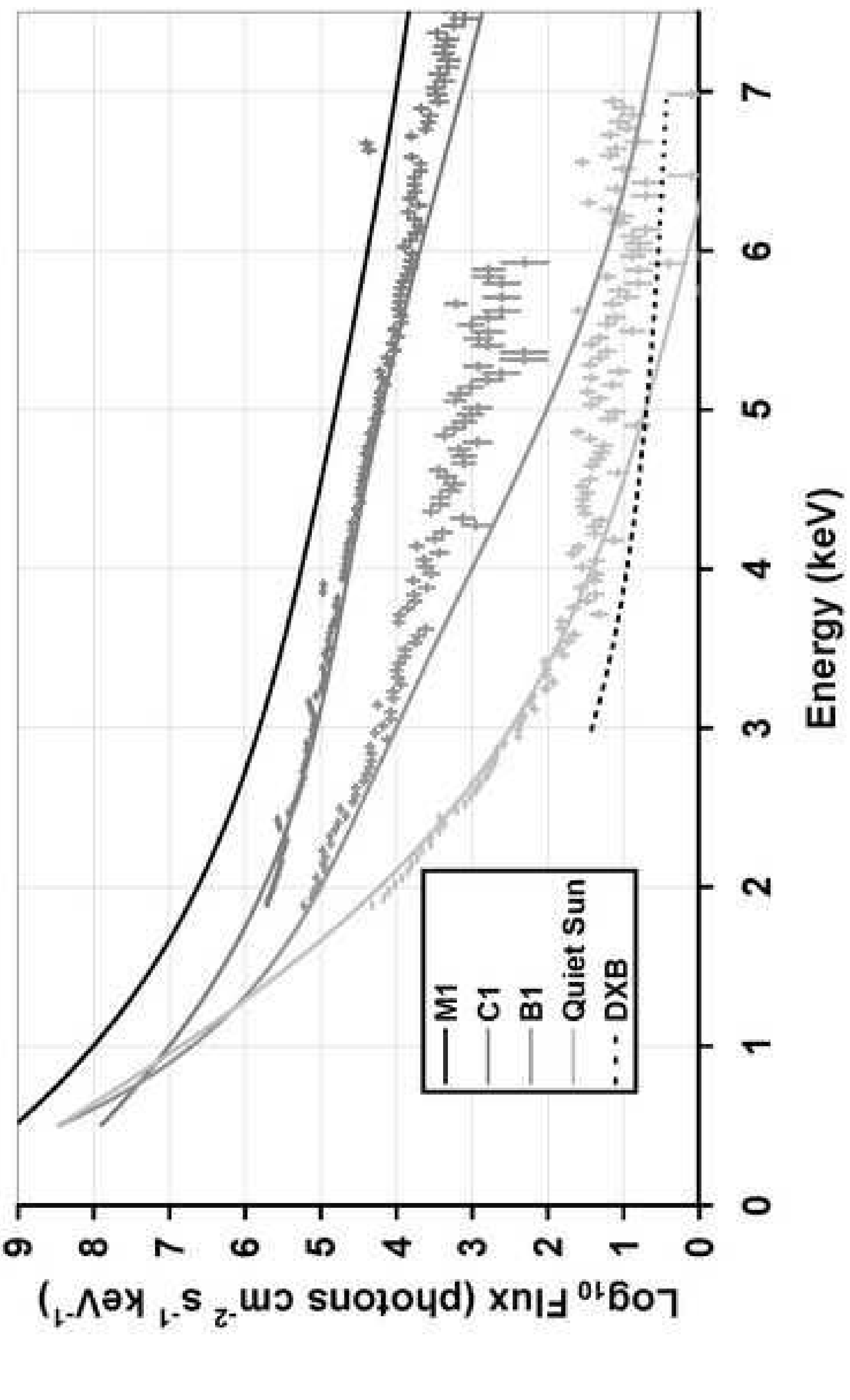
M1
C1
B1
Quiet Sun
DXB
Energy (keV)
Log10 Flux (photons cm-2 s-1 keV-1)
0
1
2
3
4
5
6
7
8
9

Figure2

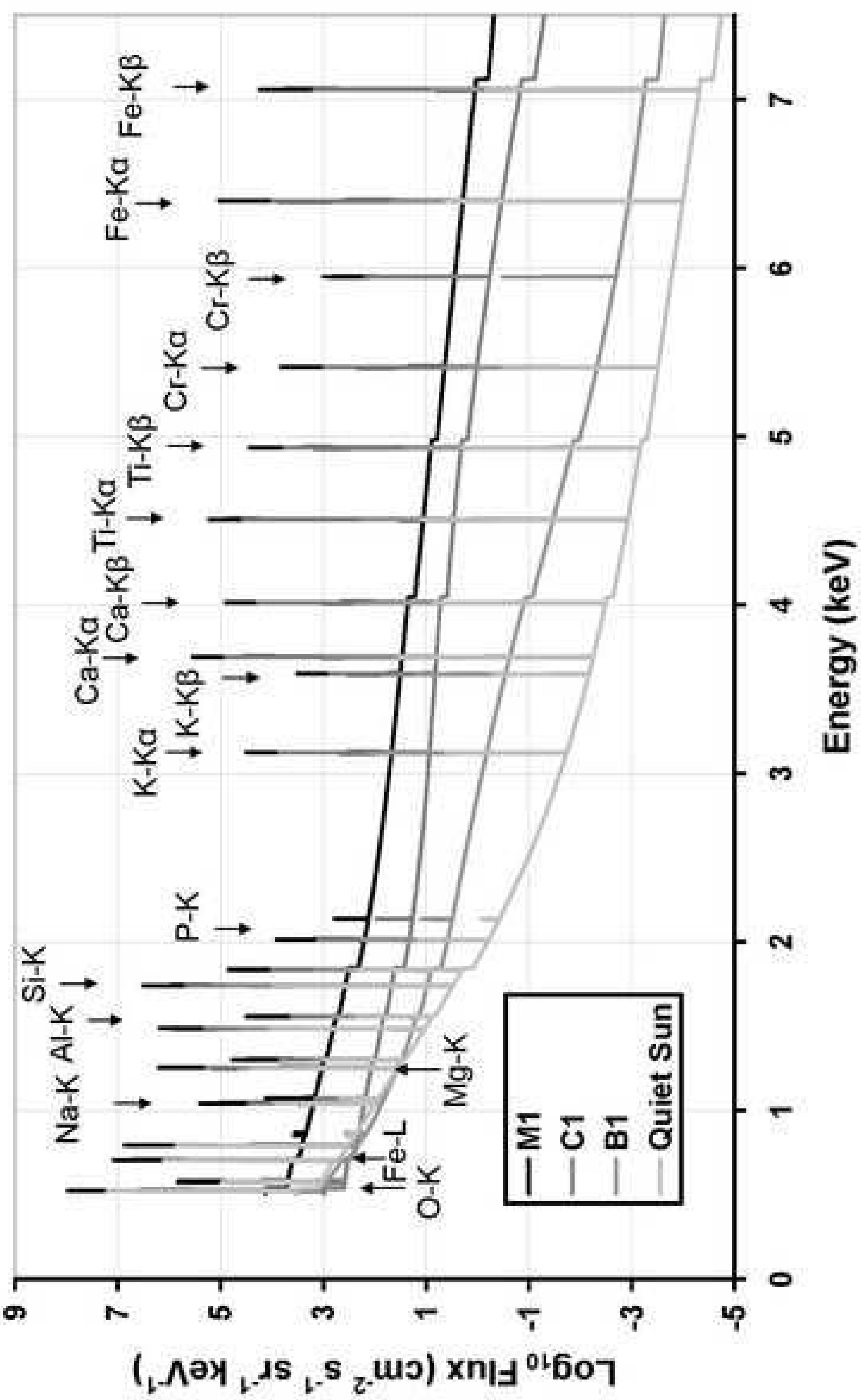

Log10 Flux (cm-2 s-1 sr-1 keV-1)
Energy (keV)
O-K
Fe-L
Na-K
Mg-K
Al-K
Si-K
P-K
K-Kα
K-Kβ
Ca-Kα
Ca-Kβ
Ti-Kα
Ti-Kβ
Cr-Kα
Cr-Kβ
Fe-Kα
Fe-Kβ
M1
C1
B1
Quiet Sun

Figure3

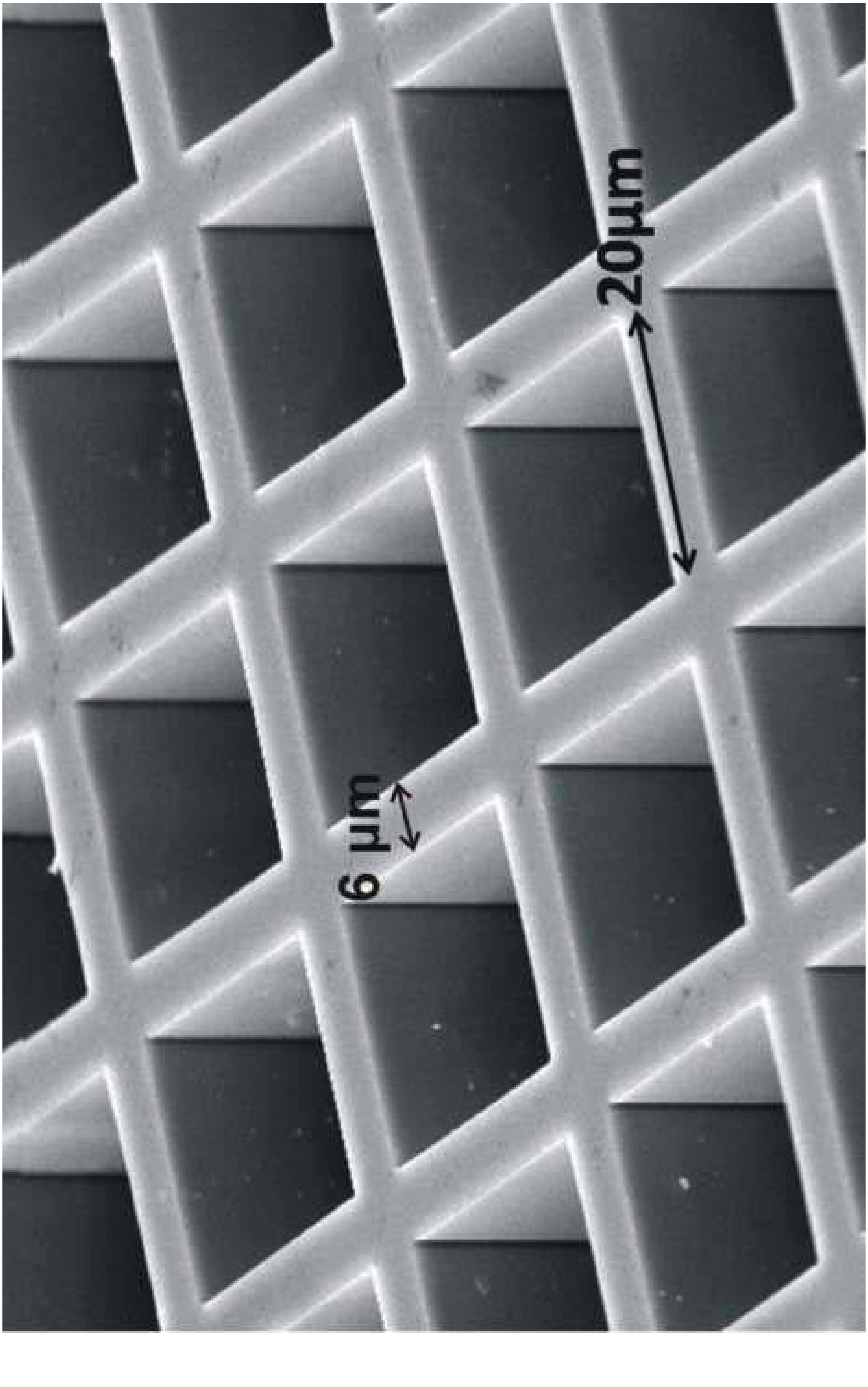

Figure 4

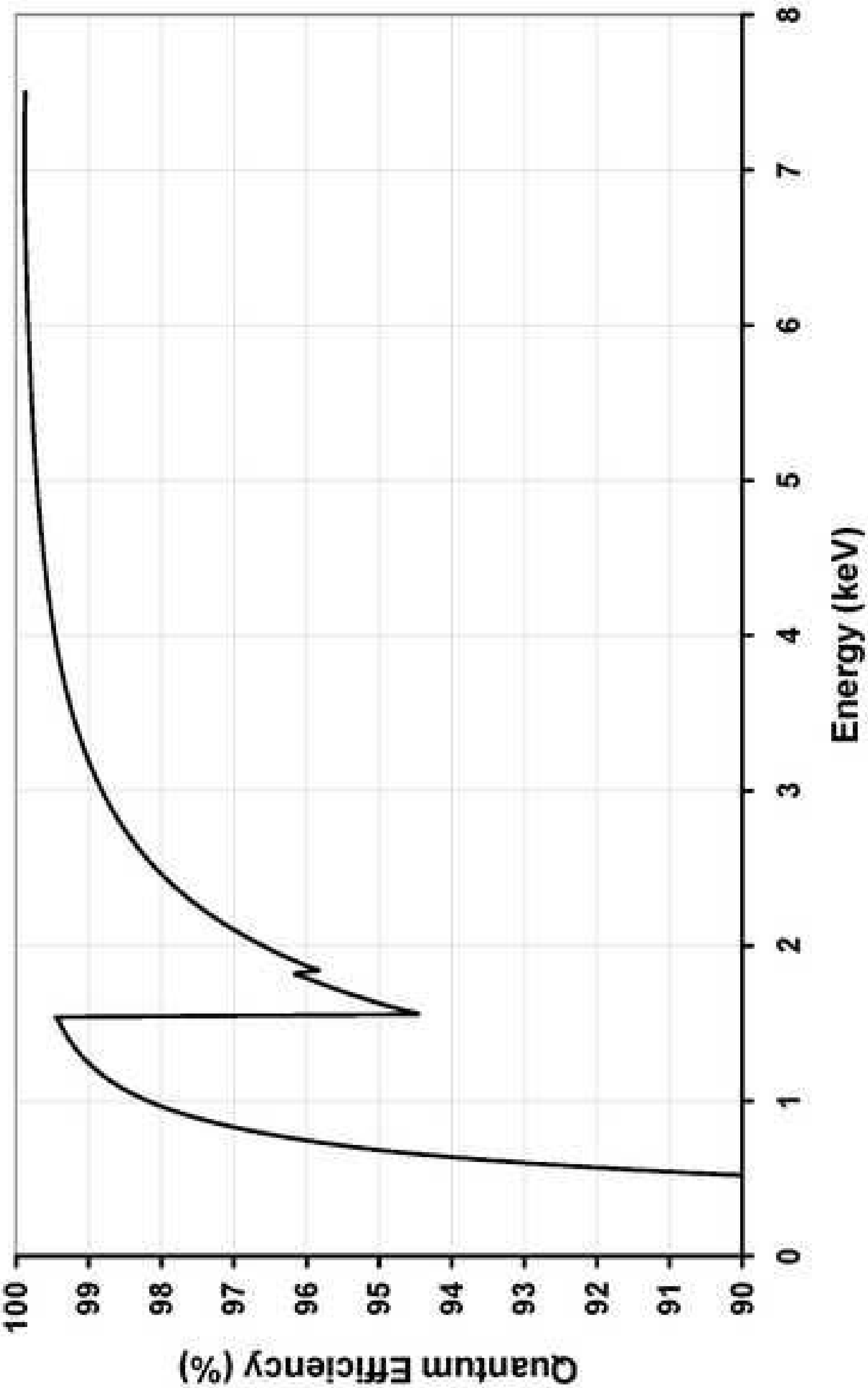
Quantum Efficiency (%)
100
99
98
97
96
95
94
93
92
91
90
Energy (keV)
0
1
2
3
4
5
6
7
8

Figure5

Figure6

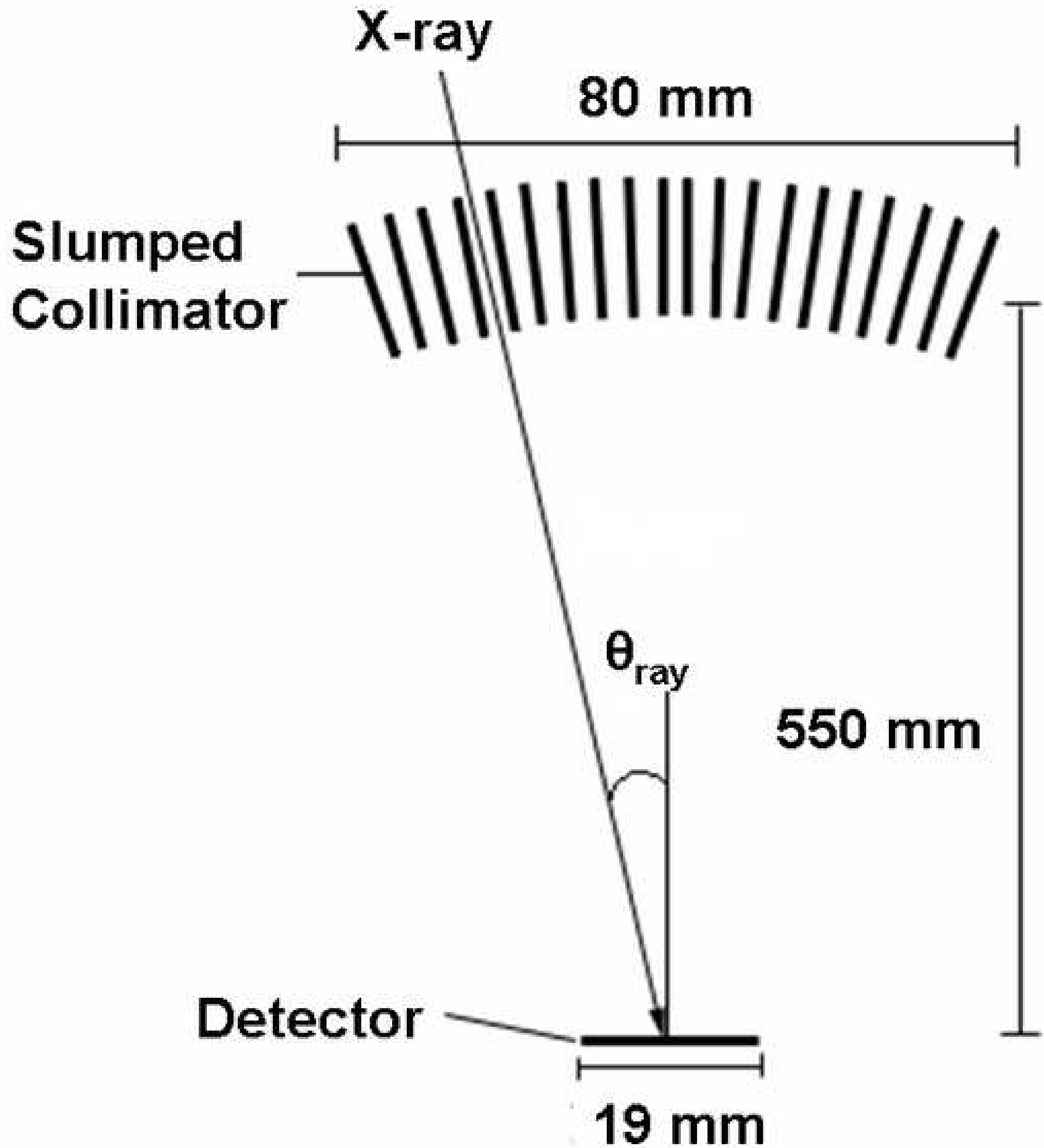

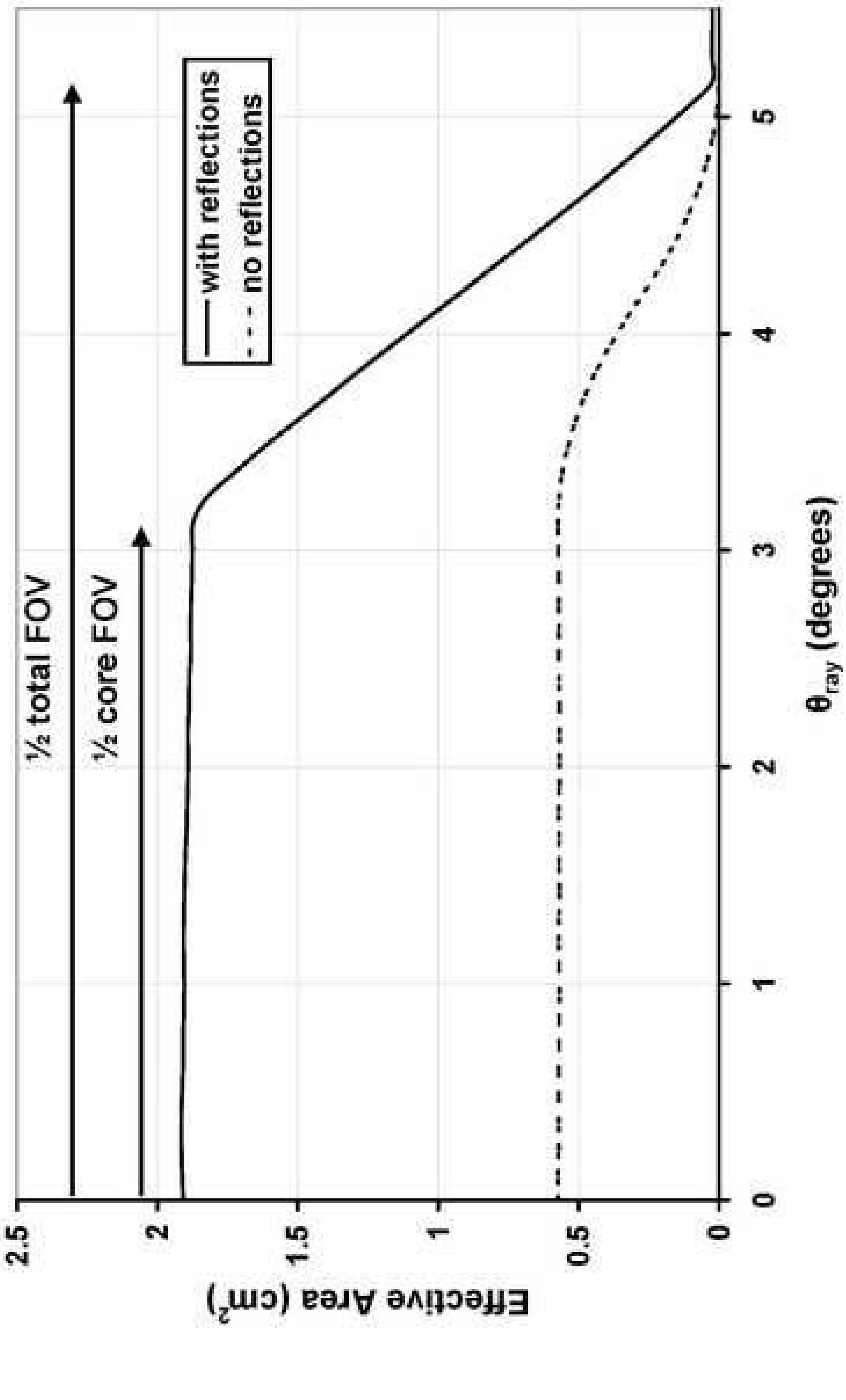
½ total FOV
½ core FOV
with reflections
no reflections
Effective Area (cm²)
2.5
2
1.5
1
0.5
0
0
1
2
3
4
5
θray (degrees)

Figure7

Figure8

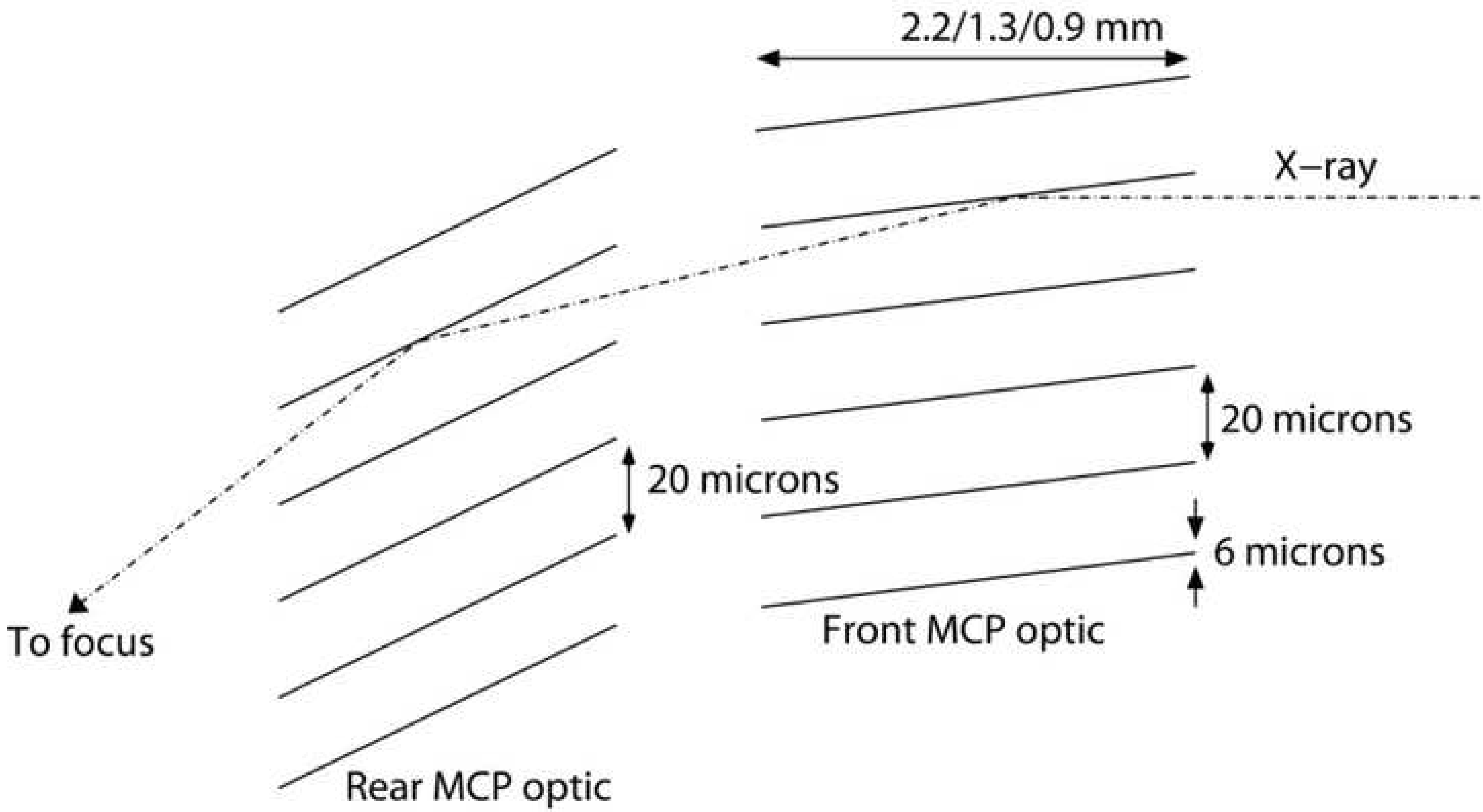
2.2/1.3/0.9 mm
X–ray
20 microns
20 microns
6 microns
Front MCP optic
Rear MCP optic
To focus

Figure9

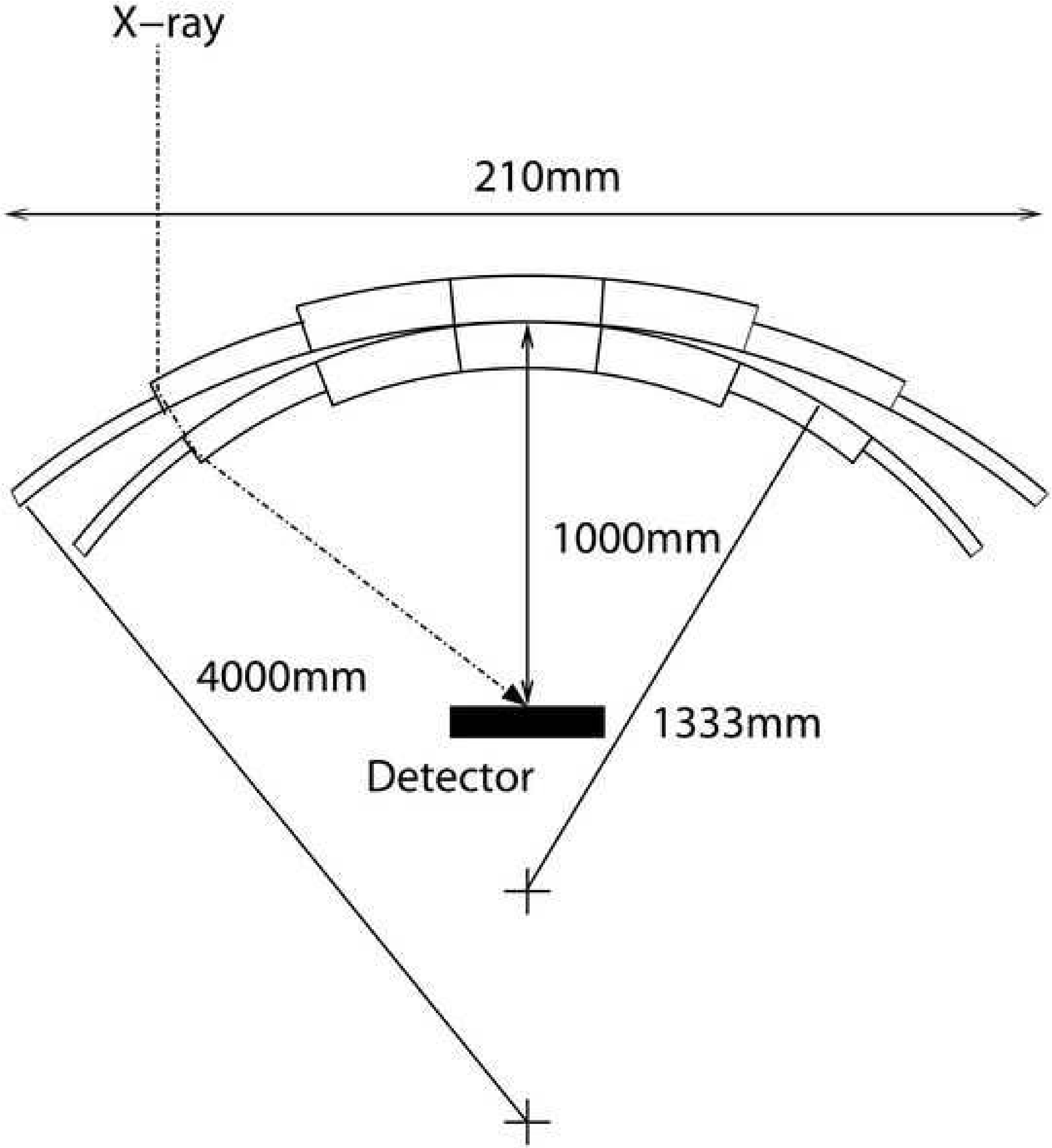

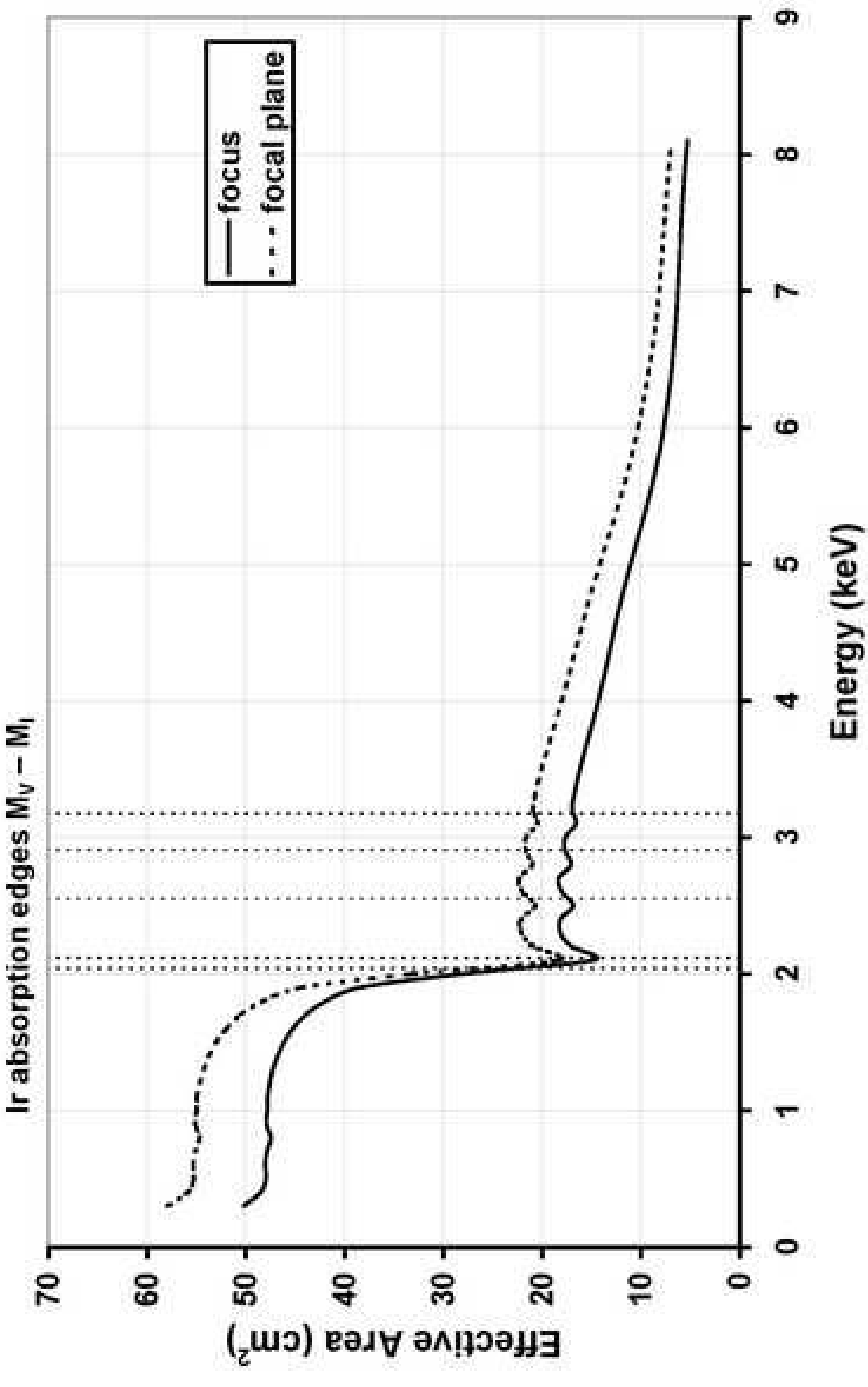
Ir absorption edges M_V – M_I
focus
focal plane
Effective Area (cm^2)
Energy (keV)
0
10
20
30
40
50
60
70
0
1
2
3
4
5
6
7
8
9

Figure10

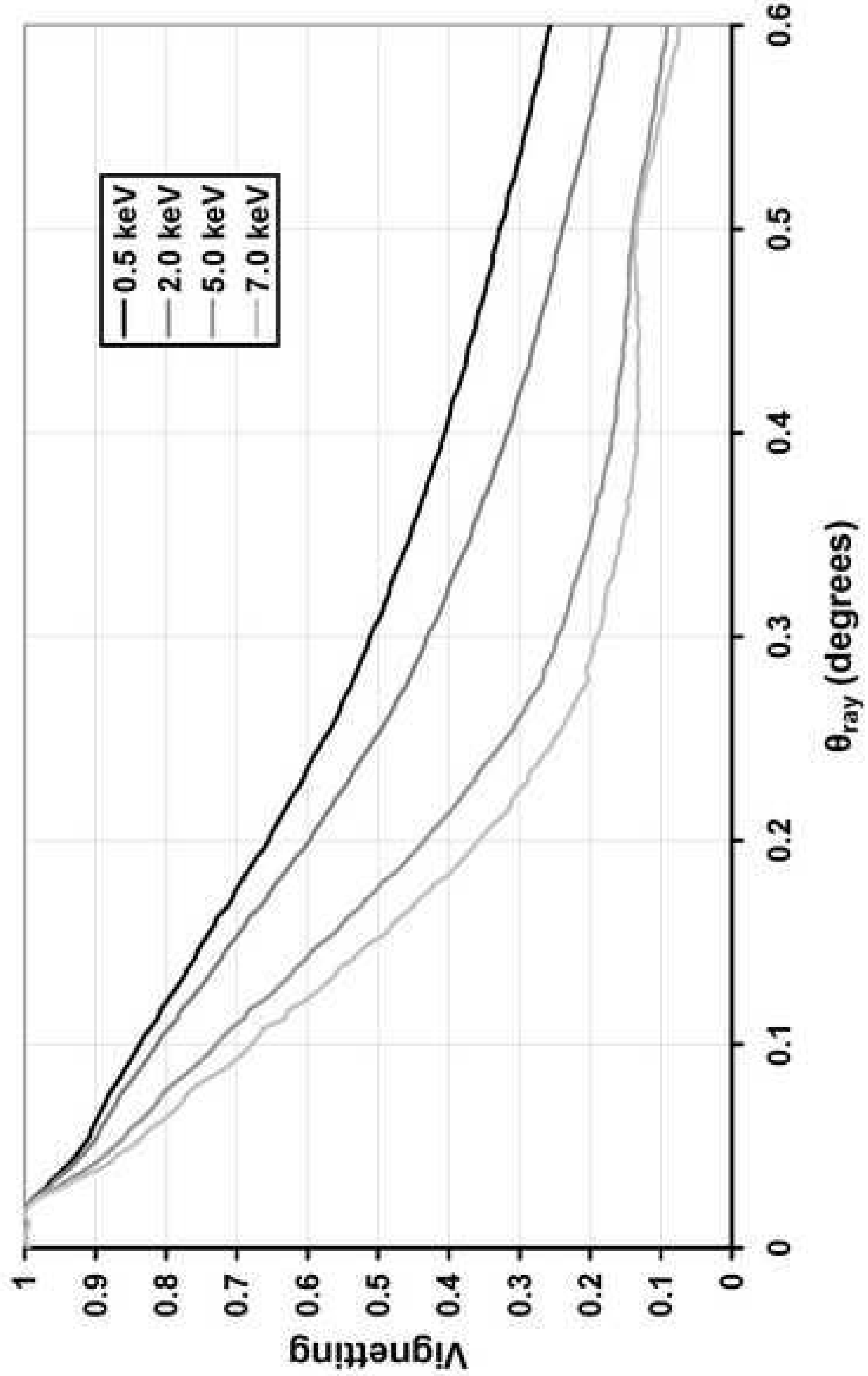

Vignetting
1
0.9
0.8
0.7
0.6
0.5
0.4
0.3
0.2
0.1
0
0
0.1
0.2
0.3
0.4
0.5
0.6
θ_{ray} (degrees)
0.5 keV
2.0 keV
5.0 keV
7.0 keV

Figure11

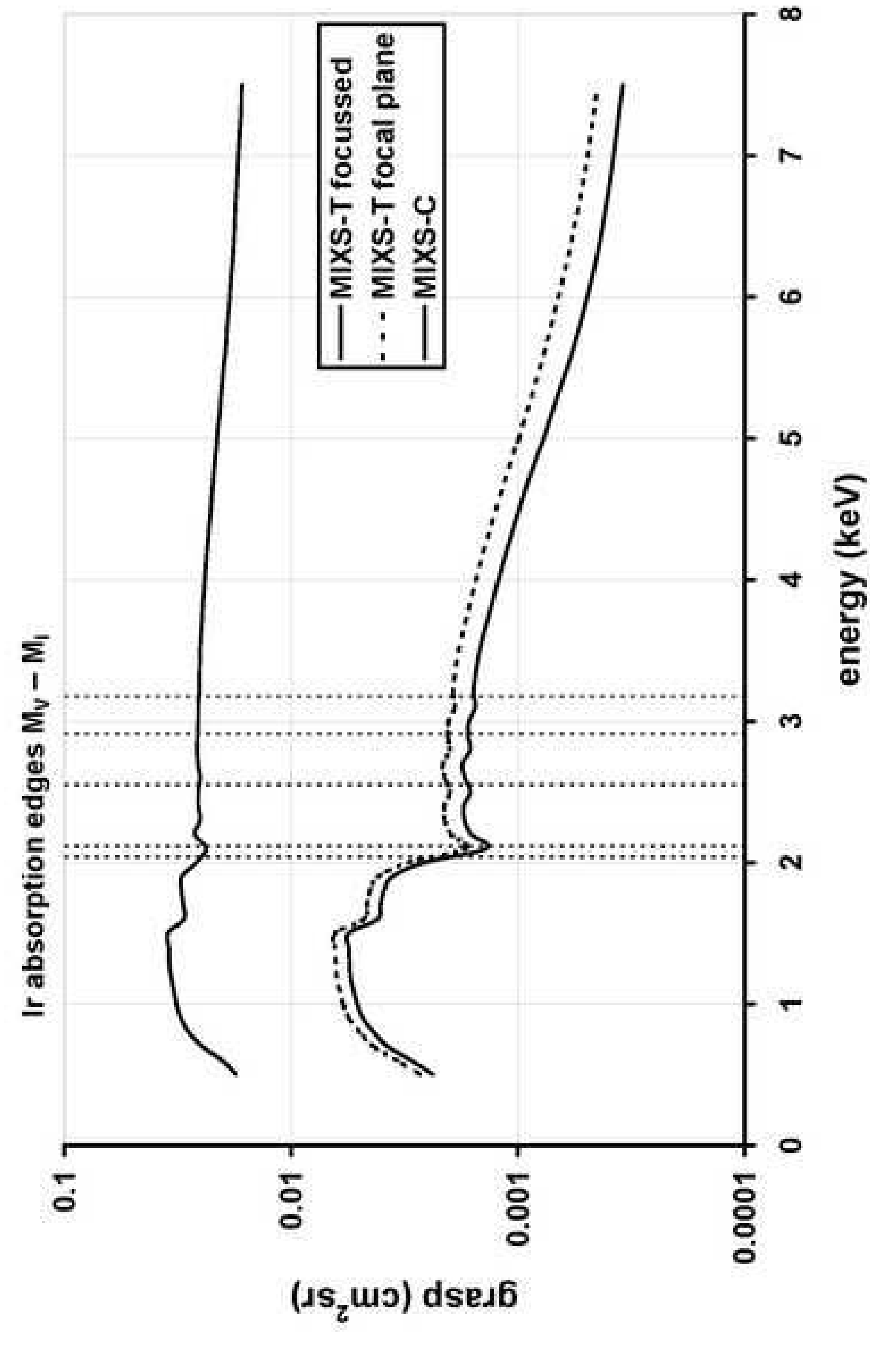
Ir absorption edges M$_V$ – M$_I$
MIXS-T focussed
MIXS-T focal plane
MIXS-C
grasp (cm^{2}sr)
0.1
0.01
0.001
0.0001
energy (keV)
0
1
2
3
4
5
6
7
8

Figure12

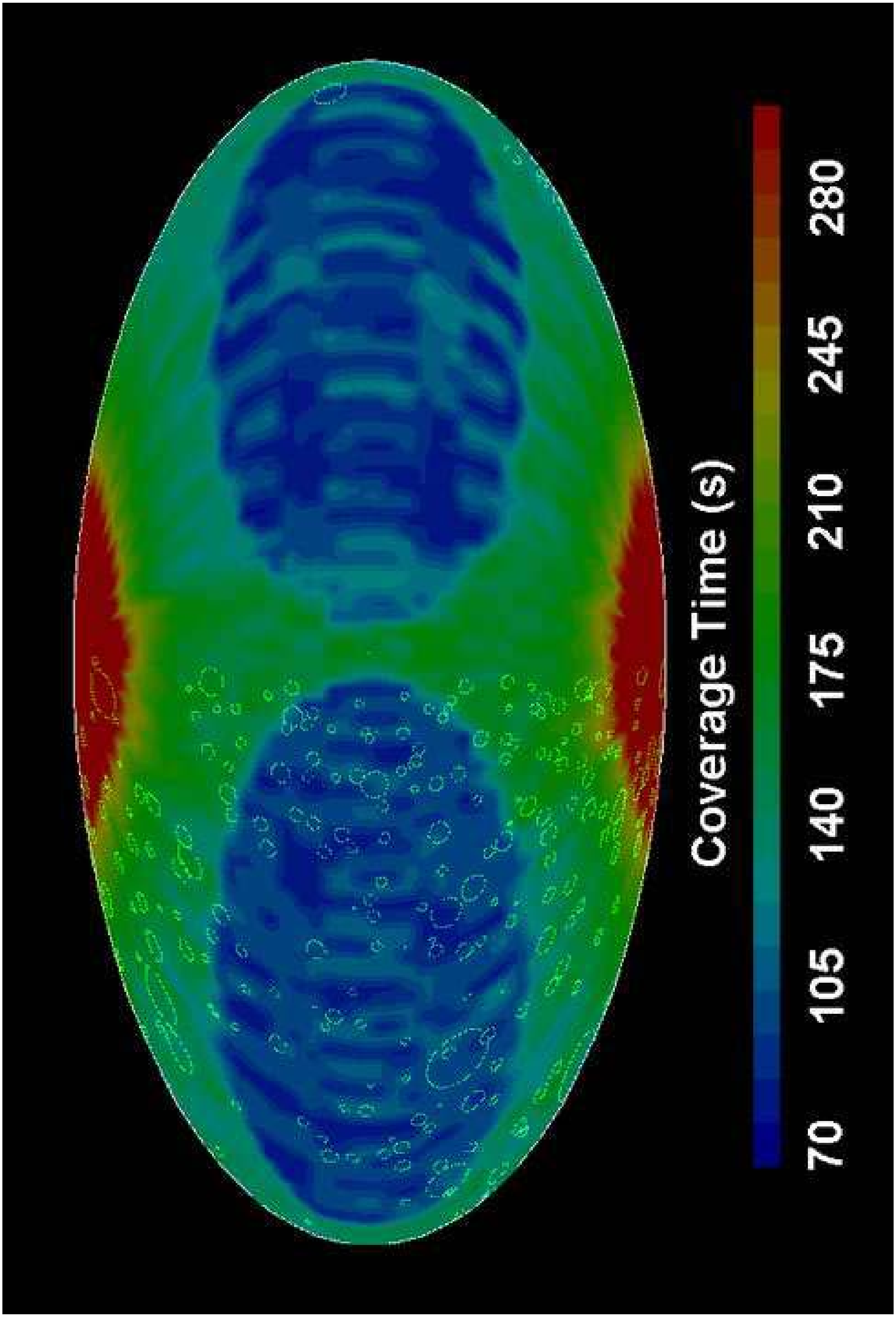

Figure13

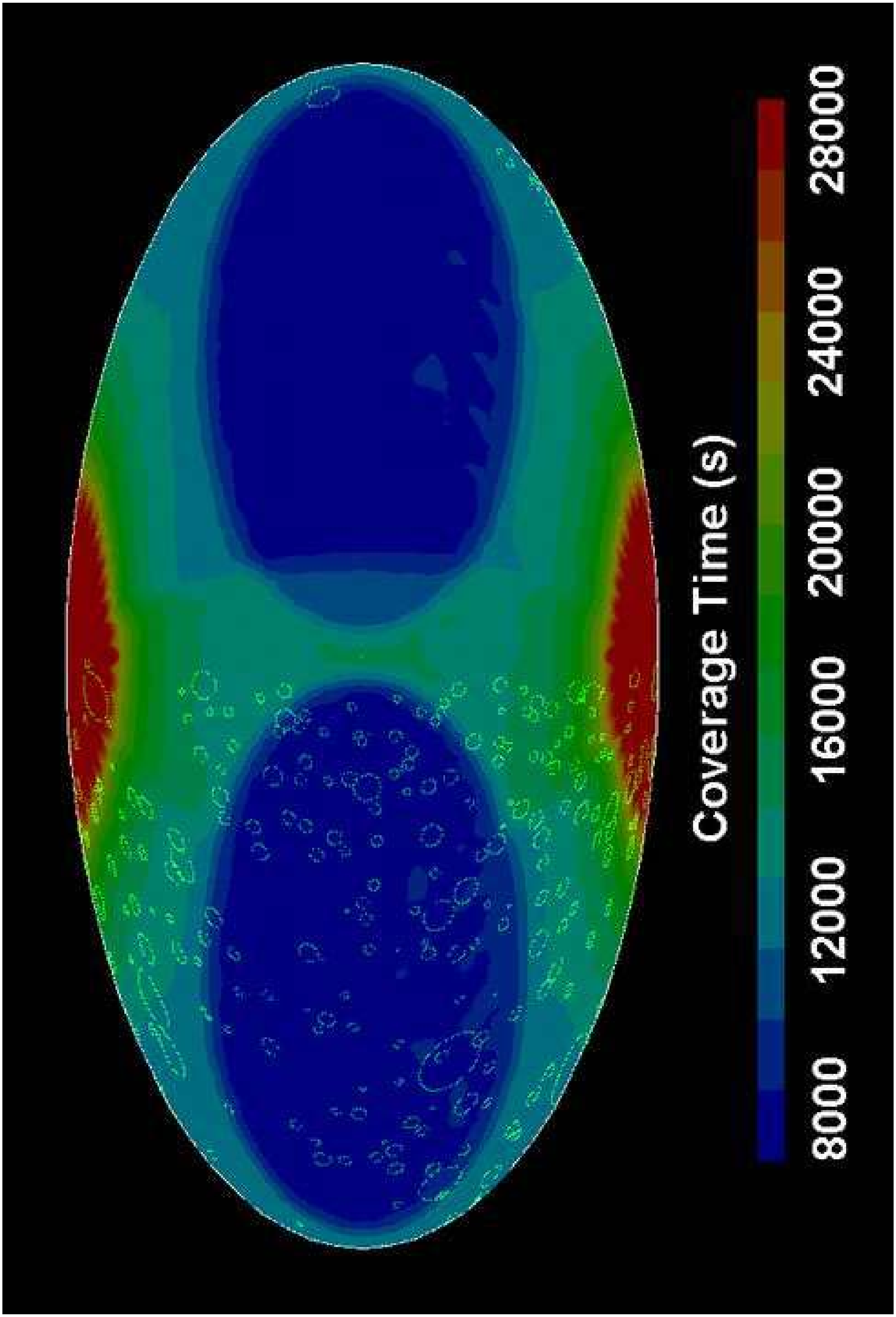

Figure14

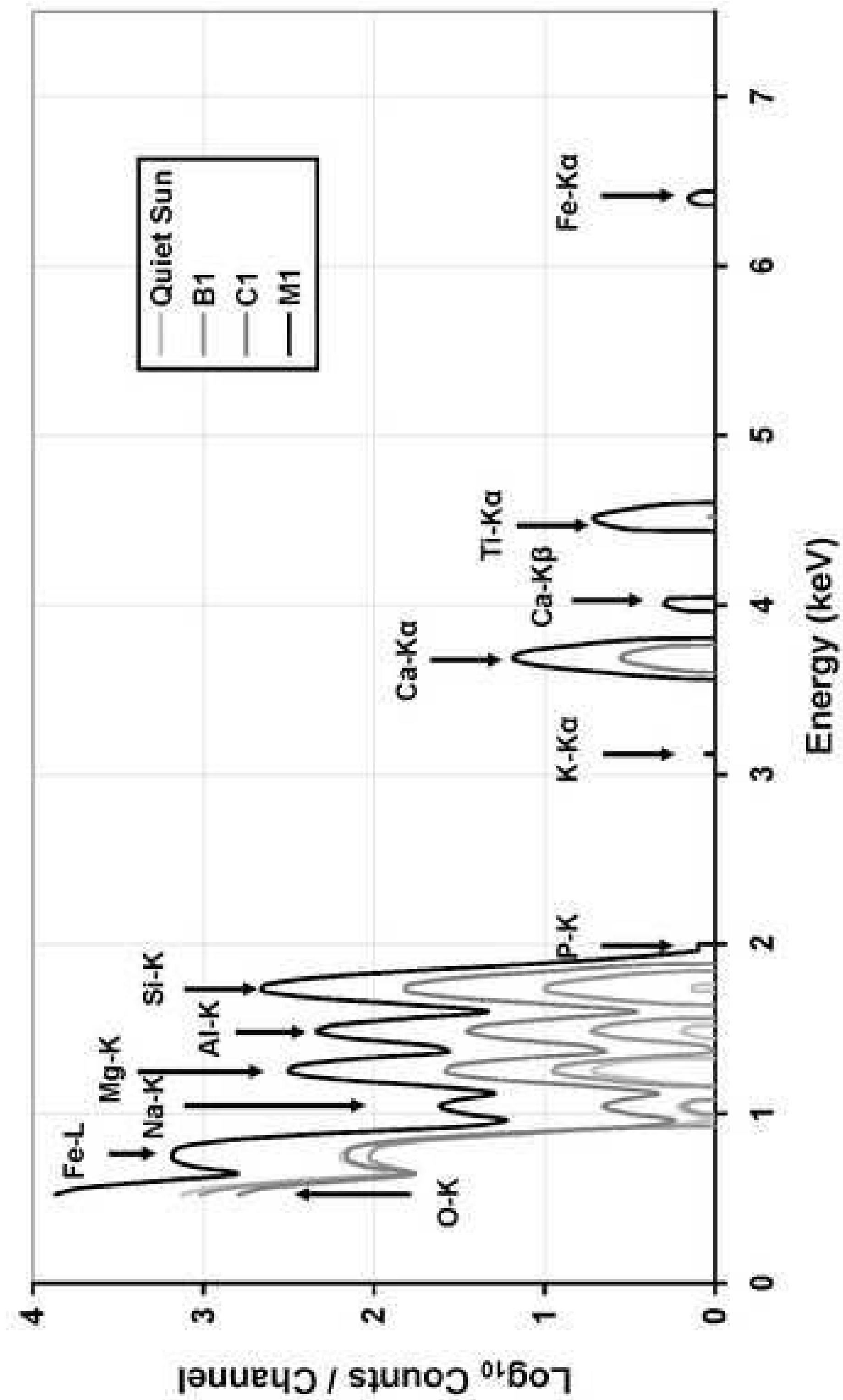
Log10 Counts / Channel
Energy (keV)
Quiet Sun
B1
C1
M1
Fe-L
O-K
Na-K
Mg-K
Al-K
Si-K
P-K
K-Kα
Ca-Kα
Ca-Kβ
Ti-Kα
Fe-Kα
0
1
2
3
4
5
6
7

Figure15

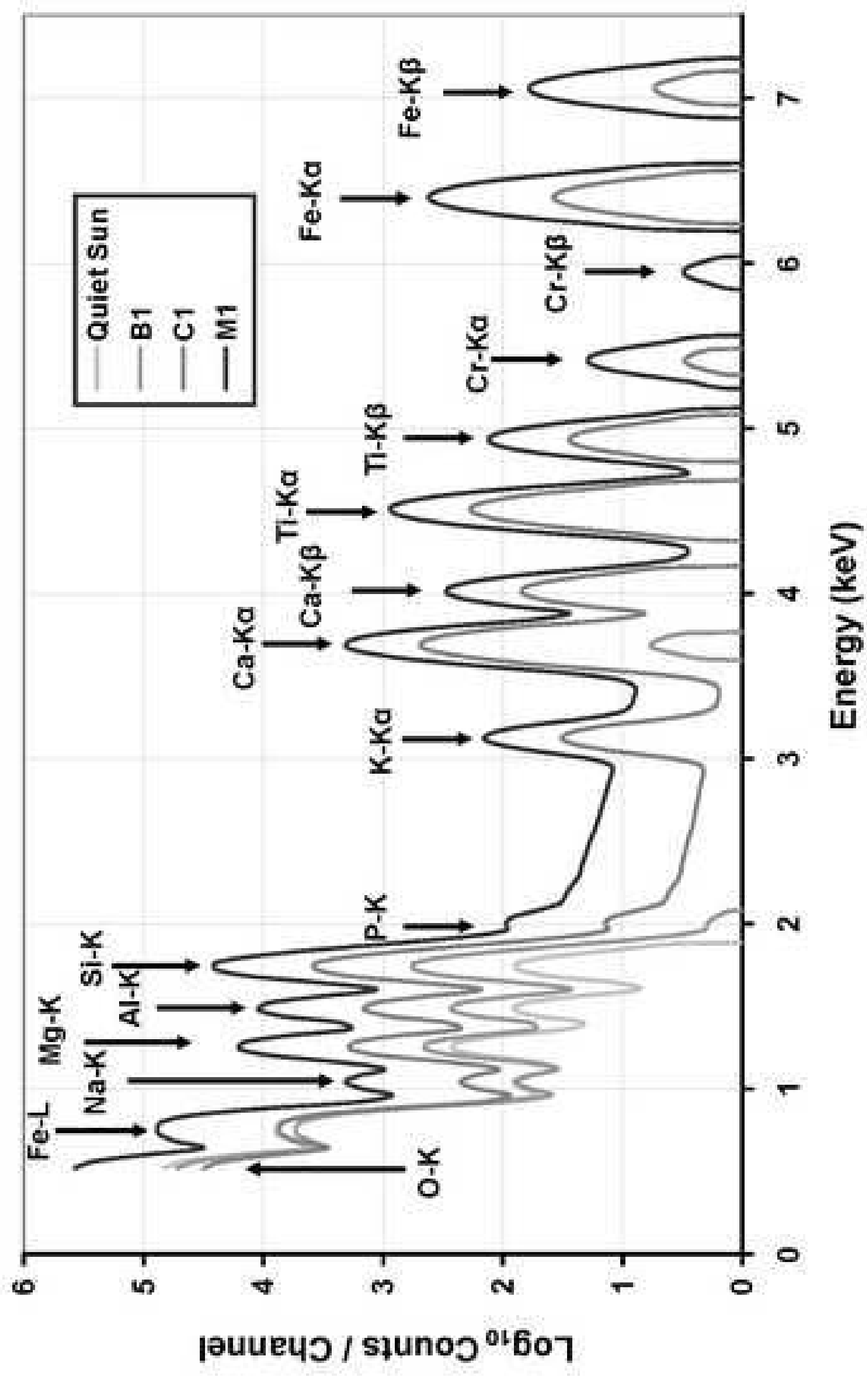
Log10 Counts / Channel
Energy (keV)
0
1
2
3
4
5
6
7
Quiet Sun
B1
C1
M1
O-K
Fe-L
Na-K
Mg-K
Al-K
Si-K
P-K
K-Kα
Ca-Kα
Ca-Kβ
Ti-Kα
Ti-Kβ
Cr-Kα
Cr-Kβ
Fe-Kα
Fe-Kβ

Figure16

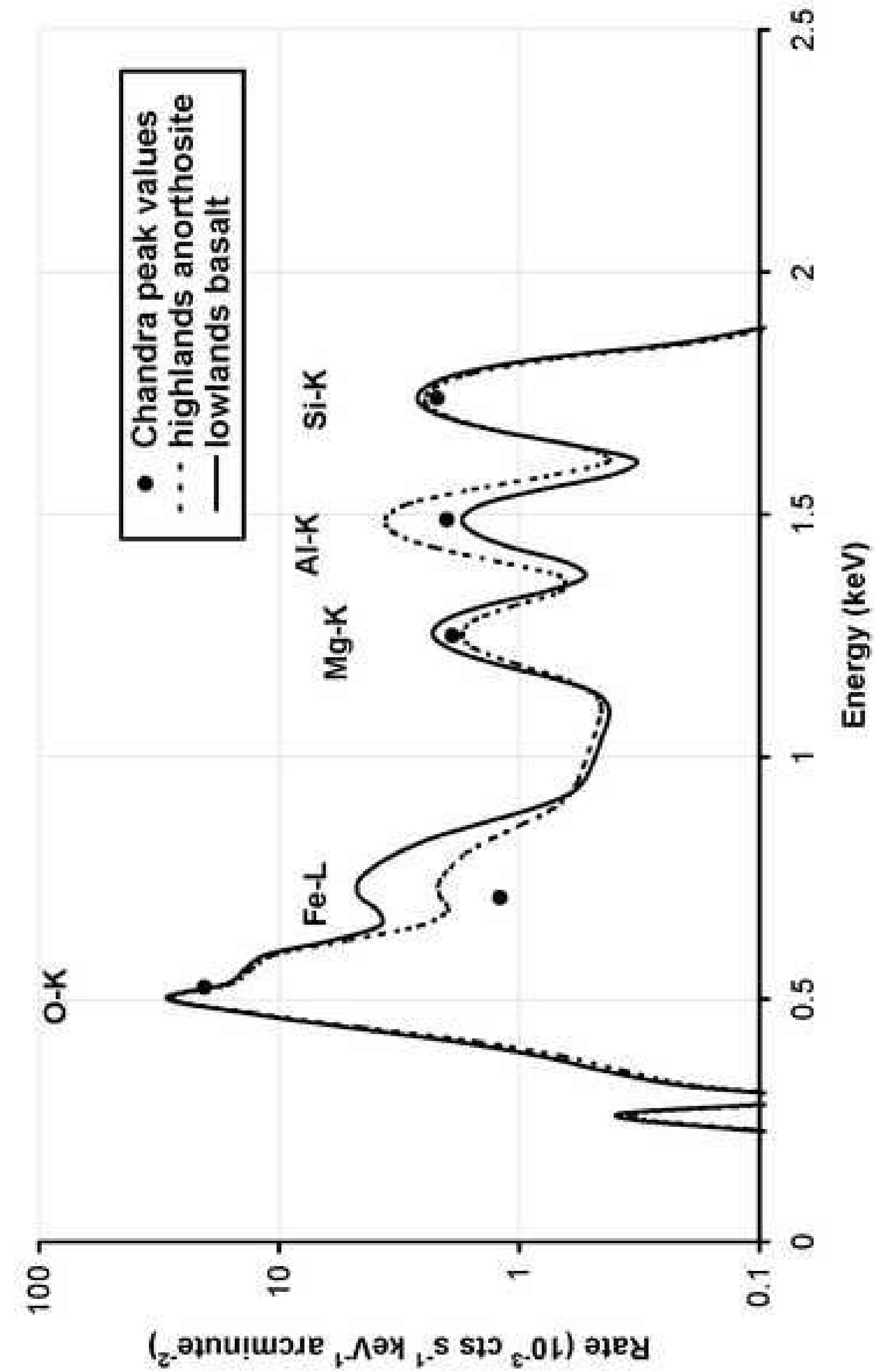
Chandra peak values
highlands anorthosite
lowlands basalt
O-K
Fe-L
Mg-K
Al-K
Si-K
Energy (keV)
Rate (10^{-3} cts s^{-1} keV^{-1} $arcminute^{-2}$)
0
0.5
1
1.5
2
2.5
0.1
1
10
100

Figure17